

# IIM METAL NEWS

(MONTHLY EDITION)

CELEBRATING PLATINUM JUBILEE OF IIM

ISSN 0972-0480

Vol. 24 No. 12

DECEMBER 2021



We make  
the best,  
even better.

JSW - A conglomerate worth \$12 Billion believes in transformation to make a better world every day

It takes a strong will to be ranked among India's top business houses. But it was stronger dreams and ambition that made us venture into the core sectors of Steel, Energy, Cement and Infrastructure. Our strength, state-of-the art technology and excellence in execution have helped us grow and that has helped India grow multi-fold. By harbouring dreams of transformation, focusing on sustainability and a philosophy: to give back to the country, the JSW Group is making a better world every day.

Steel | Energy | Infrastructure | Cement | Paints  
Ventures | Foundation | Sports  
[www.jsw.in](http://www.jsw.in)

  
Better Everyday



The Indian Institute of Metals



**Do you know why Hindalco Industries is the most sustainable aluminium company in the world?**

Because our sustainability-led operations are designed to give you **#GreenerStrongerSmarter** options for Cookware, Food & Pharma packaging, Electricals, Construction, Transport, and more!

OUR BRANDS



**Hindalco Industries Ltd.** Birla Centurion, 6th & 7th floor, Pandurang Budhkar Marg, Worli, Mumbai - 400 030, India  
T: 91 22 6662 6666/ 6261 0555/ 6266 0666 W: [www.hindalco.com](http://www.hindalco.com)

# IIM METAL NEWS

Vol. 24 No. 12

December 2021

## C O N T E N T S

<b><i>G D Birla Gold Medal Lecture - 2021</i></b> <b>Challenges and Breakthroughs in the Development of High temperature Materials</b> <b>- Rahul Mitra</b>	<b>6</b>
<b>News Updates</b>	<b>29</b>
<b>IIM Chapter Activities</b>	<b>30</b>
<b>Obituary</b>	<b>33</b>
<b>Steel Statistics</b>	<b>33</b>

The IIM Metal News and The Indian Institute of Metals do not accept any responsibility for the statements made and the opinion expressed by the author(s) in the technical articles.

Printed and Published by Shri Kushal Saha, Secretary General, on behalf of "The Indian Institute of Metals", and printed at Print Max, 44, Biplabi Pulindas Street, Kolkata-700009 • Email : printmax41@gmail.com and published at 'Metal House', Plot 13/4, Block AQ, Sector V, Salt Lake, Kolkata-700091, West Bengal, India  
E-mail: secretarygeneral.iim@gmail.com, iimmetalnews@yahoo.com Phone: 033-2367 9768 / 2367 5004

Website: [www.iim-india.net](http://www.iim-india.net) Fax: (033) 2367 5335

Facebook - <https://www.facebook.com/TheIndianInstituteofMetals/>

Instagram - <https://www.instagram.com/indianinstituteofmetals/>

LinkedIn - <https://www.linkedin.com/company/the-indian-institute-of-metals/>

Twitter - [https://twitter.com/iimetals\\_india](https://twitter.com/iimetals_india)

**Chief Editor : Dr N Eswara Prasad**

# THE INDIAN INSTITUTE OF METALS

## PATRONS

Mr R M Dastur

Dr Baba Kalyani

## ADVISORY COMMITTEE OF FORMER PRESIDENTS

Dr Dipankar Banerjee  
Mr M Narayana Rao  
Mr H M Nerurkar

Prof K Chattopadhyay  
Dr R N Patra  
Mr S S Mohanty  
Mr T V Narendran, Convenor

Prof Indranil Manna  
Dr Biswajit Basu  
Mr Anand Sen

## COUNCIL FOR THE YEAR 2021-22

### PRESIDENT

Mr T V Narendran

### VICE PRESIDENT & CHAIRMAN

#### Metal Science Division

Dr Samir V Kamat

### VICE PRESIDENT & CHAIRMAN

#### Non- Ferrrous Division

Mr Satish Pai

### VICE PRESIDENT & CHAIRMAN

#### Ferrous Division

Mr Sajjan Jindal

### IMMEDIATE FORMER PRESIDENT

Prof Amol A Gokhale

### SECRETARY GENERAL

Mr Kushal Saha

### HON TREASURER

Mr Somnath Guha

### CONTROLLER OF EXAMINATIONS

Prof P K Mitra

### CHIEF EDITOR, TRANSACTIONS

Prof B S Murty

### CHIEF EDITOR, IIM METAL NEWS

Dr N Eswara Prasad

### Jt. SECRETARY

(Office of President)

Mr Chaitanya Bhanu

### MEMBERS

Prof Amit Arora  
Dr R Balamuralikrishnan  
Dr V Balusamy  
Prof Suddhasatwa Basu  
Dr A N Bhagat  
Dr Raghavendra R Bhat  
Dr Amit Bhattacharjee  
Dr Debashish Bhattacharjee  
Dr Tanmay Bhattacharyya  
Dr S P Butee  
Dr Indranil Chattoraj  
Mr B K Das  
Mr Prem Ganesh  
Mr Kanak Kumar Ghosh  
Prof Dipti Gupta  
Dr S K Jha  
Mr Kishore Kumar Mehrotra

Mr Arun Mishra  
Prof B K Mishra  
Mr Bibhu Prasad Mishra  
Dr Suman Kumari Mishra  
Prof Sushil K Mishra  
Prof Rahul Mitra  
Ms Soma Mondal  
Dr S V S Narayana Murty  
Mr M K Murugan  
Mr K Nagarajan  
Dr Vinod Nowal  
Mr Dilip Oommen  
Mr Ambika Prasad Panda  
Mr Sudhanshu Pathak  
Dr Divakar Ramachandran  
Dr Asim K Ray  
Dr G Madhusudhan Reddy

Mr Barun Roy  
Mr Bhaskar Roy  
Prof Rajiv Shekhar  
Dr Bimal P Singh  
Dr Arijit Saha Podder  
Dr S Savithri  
Shri Sanjay Sharma  
Mr Arun Kumar Shukla  
Prof Amarendra Kumar Singh  
Mr Brijendra Pratap Singh  
Mr Lokendra Raj Singh  
Dr T Sundararajan  
Mr G Surendra  
Prof Satyam Suwas  
Dr Vilas Tathavadkar  
Dr M Vasudevan  
Dr P V Venkitakrishnan

## FORMER PRESIDENTS

1946-48	Late J J Ghandy	1977-78	Late V A Altekar	1992-93	Late A C Wadhawan	2007-08	Late Srikumar Banerjee
1948-50	Late P Ginwala	1978-79	Late T R Anantharaman	1993-94	Late R Krishnan	2008-09	Mr L Pugazhenthay
1950-52	Late Phiroz Kutar	1979-80	Late P L Agrawal	1994-95	Dr S K Gupta	2009-10	Dr Sanak Mishra
1952-54	Late G C Mitter	1980-81	Late EG Ramachandran	1995-96	Mr R N Parbat	2010-11	Dr D Banerjee
1954-56	Late M S Thacker	1981-82	Late C V Sundaram	1996-97	Late P Rodriguez	2011-12	Mr M Narayana Rao
1956-58	Late K S Krishnan	1982-83	Late Samarjungavan	1997-98	Late S Das Gupta	2012-13	Mr H M Nerurkar
1958-60	Late S K Nanavati	1983-84	Late J Marwaha	1998-99	Dr C G K Nair	2013-14	Prof K Chattopadhyay
1960-62	Late G K Ogale	1984-85	Late A K Seal	1999-00	Prof S Ranganathan	2014-15	Dr R N Patra
1962-65	Late Dara P Antia	1985-86	Dr J J Irani	2000-01	Mr V Gujral	2015-16	Mr S S Mohanty
1965-67	Late B R Nijhawan	1986-87	Late Y M Mehta	2001-02	Late P Parvathisem	2016-17	Prof Indranil Manna
1967-70	Late M N Dastur	1987-88	Dr V S Arunachalam	2002-03	Late P Ramachandra Rao	2017-18	Dr Biswajit Basu
1970-72	Late Brahm Prakash	1988-89	Late S R Jain	2003-04	Dr S K Bhattacharyya	2018-19	Mr Anand Sen
1972-74	Late P Anant	1989-90	Late L R Vaidyanath	2004-05	Dr T K Mukherjee	2019-20	Dr U Kamachi Mudali
1974-76	Late FAA Jasdhanwalla	1990-91	Dr P Rama Rao	2005-06	Late Baldev Raj	2020-21	Prof Amol A Gokhale
1976-77	Late S Visvanathan	1991-92	Dr T Mukherjee	2006-07	Mr B Muthuraman		

## FORMER SECRETARIES / SECRETARY GENERALS\*

1946-57	Late Dara P Antia	1968-76	Dr M N Parthasarathi	1986-97	Late S S Das Gupta	2006-13	*Mr J C Marwah
1958-67	Mr R D Lalkaka	1977-86	Late L R Vaidyanath	1997-06	Mr J C Marwah	2013-15	*Mr Bhaskar Roy
						2015-18	*Mr Sadhan Kumar Roy

# RINL-Vizag Steel... Strengthening the New India



सही से मास्क पहनें | हाथ धोएँ बार बार | निभाएँ दो गज की दूरी

कोरोना से बचें  
जब तक दवाई नहीं  
तब तक ढिलाई नहीं

Associated with projects of national importance



RINL - Vizag Steel is proud to be associated with ATAL Tunnel the longest highway tunnel at a height of 10,000 ft. Supplied major share of TMT requirements (8500 MT of Vizag Steel TMT Rebars)

#### AIRPORTS

Bangalore, Kochi, Delhi, Hyderabad, Mumbai & Chandigarh

#### METRO RAIL

Delhi, Hyderabad, Kolkata, Chennai, Jaipur, Mumbai, Kochi & Nagpur, Pune

#### NUCLEAR POWER PLANTS

Kudamkulam, Kaiga, Tarapore

#### THERMAL POWER PLANTS

Dhabol, Rajpura

#### NATIONAL HIGHWAYS

Yamuna Expressway, Ahmedabad-Vadodara Expressway, Eastern Freight Corridor, Mumbai-Pune Express way

#### HYDRO-ELECTRIC POWER PROJECTS

Alakananda, Sardar Sarovar

#### ❖ Bandra-Worli Sea Link Bridge, Mumbai

❖ Visakhapatnam Port Trust

## उत्पाद श्रेणियाँ व उपयोग PRODUCT MIX & APPLICATIONS



WIRE RODS

5.5mm - 20mm

Wire drawing, Bright bars, Fasteners etc.



ROUNDS

16 - 95mm 20-45mm both Straight & Coil form  
45-95mm straight length

Fasteners, Forging, Re-rolling, Railways, Construction



VIZAG TMT REBARS

8mm - 36mm

Construction - Reinforcement



BILLETS / BLOOMS

65mm, 77mm, 90 mm / 150mm, 200mm

Bright bars, Forging, Re-rolling, General Engineering purposes



VIZAG UKKU STRUCTURALS

Angles 75 x 75 x 6 - 110 x 110 x 10mm  
Channels 100 x 50 - 200 x 75mm  
Beams 125 x 70 - 150 x 75mm  
Flats 80 x 12 - 100 x 20mm

Construction, Fabrication, Auto Leaf Springs

f @RINL VIZAG STEEL @RINL\_VSP r.i.n.l

www.vizagsteel.com

राष्ट्रीय इस्पात निगम लिमिटेड  
(भारत सरकार का उद्यम)  
विशाखपट्टणम इस्पात संयंत्र

ISO 9001:2015, ISO 14001, ISO 50001, ISO 27001 & OHSAS 18001 Certified Company

## Challenges and Breakthroughs in the Development of High temperature Materials



### Rahul Mitra

Professor, Department of Metallurgical and Materials Engineering  
Indian Institute of Technology Kharagpur, Kharagpur – 721302, West Bengal

#### Abstract

In order to achieve higher energy efficiency and superior performance of engineering components in automotive and aero-engines, thermal and nuclear power industries, various industrial operations, as well as extreme environments experienced in service similar to that by nose-cones and leading edges of hypersonic vehicles, there has been a strong drive for research and development of high temperature materials. High melting point, phase stability, structural integrity and the ability to retain yield and creep strength at high temperature along with a strong resistance to environmental degradation, besides a reasonable amount of fracture toughness or damage tolerance are considered desirable for such materials. The strategies to improve the high temperature capabilities include suitable alloying additions, precipitation and dispersion hardening, addition of ceramic reinforcement, design and use of single crystals, as well as thermomechanical processing. Some of the breakthroughs achieved through these approaches in order to meet the challenges of high temperature materials development will be discussed in the present lecture. A significant increase in creep rupture duration along with decrease in creep rate at temperatures up to 300 °C has been noticed in

the in-situ Al<sub>4.5</sub>Cu-5TiB<sub>2</sub> composite subjected to mushy-state rolling with prior cold rolling to achieve 30% reduction. Further, precipitation of secondary carbides and their ability to pin the dislocations have been found to contribute to a steady state stage in the tertiary creep regime of the IN617 alloy at 750 and 800 °C, which in turn has extended the rupture life. In research on single crystal Ni-based superalloys, use of the <100> orientation for load application besides suitable alloying additions and heat treatment, has been found to play a key role. Multiphase alloys based on Mo and Nb silicides possess superior high temperature capabilities beyond that of the Ni-based superalloys, with strength retention and oxidation resistance being contributed by the silicide phase, and room temperature toughness by the ductile phase. Alloying of the 76Mo-14Si-10B alloy by Zr has been found to refine the grain size, aiding in rapid formation of a stable and protective borosilicate scales, thereby improving the oxidation resistance in dry or moist air. In a similar manner, addition of Ti to the Nb-Si – Mo based alloys along with annealing for 100 h at 1500 °C has altered the microstructure with significant increase in room temperature fracture-toughness, whereas presence of Mo and Ti together has improved both high temperature

strength and oxidation resistance. The ZrB<sub>2</sub>-SiC composite-based ultra-high temperature ceramic (UHTC) composites have been found to withstand temperatures >2000 °C without significant damage. Pressure-less sintering has been developed as a process to fabricate near-net and complicated shapes. Addition of Si<sub>3</sub>N<sub>4</sub> to ZrB<sub>2</sub>-SiC composites has been found to improve room temperature strength, fracture toughness and oxidation resistance but lower the high temperature creep resistance. On the other hand, addition of ≥ 10 vol% LaB<sub>6</sub> is found to significantly improve the oxidation resistance in the range of 1300-1500 °C by forming a protective scale. The mechanisms of formation of protective scale for oxidation resistance in Mo and Nb silicide-based alloys, as well as the aforementioned UHTCs have been investigated thoroughly, which may help in further development of these materials.

## 1. Introduction

I begin by sincerely thanking the Indian Institute of Metals for bestowing on me the honour of G.D. Birla Gold lecture. From the days of my undergraduate studies at IIT Kharagpur, and graduate research at Northwestern University, Evanston, Illinois, USA under the guidance of Prof. Morris E. Fine and Prof. Julia Weertman, I have felt an excitement for working on alloys and composites for high temperature applications. Today, I will like to share some of the recent exciting results obtained of my research group at IIT Kharagpur, based on the background of my work carried out earlier as Scientist at DMRL, Hyderabad.

It is well-known that the most desirable properties of materials for use at high temperatures are high melting points, ability to retain strength at the temperature of use, and high creep resistance. Additionally, for materials subject to thermal cycles or gradients, resistance to damage by thermal shock is a necessity. As the environmental degradation sets a major limitation for use at high temperatures in air or corrosive environments, the resistance to oxidation and hot corrosion is an absolute necessity. Furthermore, the ablation resistance is considered essential for use in nose-cones and leading edges of re-entry of space

vehicles. The ascending order of materials based on their high temperature capabilities is as follows: Alloy based metal matrix composites (≤ 300 °C), Ti alloys and gamma aluminides, 9Cr-1Mo and stainless steels (≤ 650 °C), Ni- and Co-based superalloys (≤ 1100 °C), Mo, W and Nb based refractory alloys as well as their silicide based multiphase alloys and Cf/SiC composites (≤ 1350 °C), MoSi<sub>2</sub> (≤ 1700 °C), ZrB<sub>2</sub> and HfB<sub>2</sub> based ultra-high temperature ceramic composites (≤ 1600 °C for long duration, and ≤ 2200 °C for short duration), and C<sub>f</sub>/C composites (≤ 2500 °C in vacuum or inert atmosphere only). The research on these high temperature materials is driven by their major applications at different temperature ranges, which include automotive engines, diesel engine glow plugs, boiler tubes and steam turbines in regular and ultra-supercritical power plants, fuel tubes of nuclear reactors, rocket nozzles, hot-end aero engine components, as well as nose-cones and leading edges of hypersonic vehicles.

The strategies to improve the retention of strength at high temperature include alloying for solid solution strengthening, precipitation hardening, dispersion strengthening, evolution of creep resistant phase in a multiphase alloy, design of metal matrix composites with suitable reinforcements, thermo-mechanical processing, and development of single crystal alloys. My research has involved the aforementioned approaches for enhancing the high temperature capabilities without compromising the oxidation resistance along with room temperature toughness. Some interesting results obtained in evaluation of the high temperature properties of selected materials have been discussed, which may contribute to further development.

## 2. Research on materials development

### 2.1 Mushy state rolled in-situ Al-4.5Cu-5TiB<sub>2</sub> composite

The process for preparing in-situ Al-TiB<sub>2</sub> composite by mixed salt reaction process was developed at IIT Kharagpur by research group headed by Prof. M. Chakraborty and Prof. B.S. Murty [1]. A major problem encountered

in processing cast Al-alloy based metal matrix composites is dendritic structure with segregation of solute at inter-dendritic locations, and distribution of reinforcement particles to form a grain boundary network, which lead to unsatisfactory mechanical properties. Keeping this problem in mind, a process for rolling of the as cast in-situ Al-4.5Cu-5TiB<sub>2</sub> composite with 20 vol% liquid content to 5% thickness reduction has been developed, which led to significant microstructural refinement with formation of equiaxed grain structure and a more uniform distribution of TiB<sub>2</sub> particles (Fig. 1(a)), which leads to improvement of mechanical properties [2,3]. It has been further noticed that the composite subjected to mushy state rolling with prior cold rolling for 30% reduction (PCMRC) has exhibited the formation of elongated grain structure with a greater number fraction of low angle boundaries, and the best possible distribution of TiB<sub>2</sub> and CuAl<sub>2</sub> particles (Fig. 1(b)), which in turn has significantly improved both tensile strength and ductility at room temperature [4]. As shown in Fig. 1(c), the creep tests on the PCMRC at 275 °C have shown the lowest steady state creep rate with time to rupture of 904 h, which is about three times more than that of mushy state rolled (MRC) and hot rolled composites (HRC) [5]. Additionally, the time to rupture observed for the PCMRC at 300 °C (260 h) is found to be more by two orders

compared to those obtained for both MRC and HRC, as shown in Fig. 1(d). It is found that a large number of low angle boundaries and more evenly distributed CuAl<sub>2</sub> and TiB<sub>2</sub> particles obtained in the PCMRC are considered responsible for higher strength and ductility at room temperature, as well as improved creep resistance at high temperature.

## 2.2 Ni-based superalloy

### 2.2.1. Non-classical creep behaviour of IN 617 alloy

Creep tests on the IN617 alloy at temperatures in the range of 650 – 800 °C have shown (i) creep curves indicating non-classical creep behaviour with a distinct steady state stage with a locally minimum and constant creep rate in the tertiary part of the creep curve at 750 and 800 °C (Fig. 2(a-b)); as well as (ii) values of apparent stress exponent (n) much higher greater than 4-5 (Fig. 2(c)), which is expected for dislocation-climb controlled creep [6]. By plotting the (creep rate)<sup>1/n</sup> against the applied stress (α), followed by extrapolation of the best-fit line to α = 0, the values of threshold stress (α<sub>0</sub>) at different temperatures have been obtained (Fig. 2(d)). Based on the results obtained from transmission electron microscopy, the threshold stress is ascribed to the interaction of dislocations with γ' precipitates and M<sub>23</sub>C<sub>6</sub> particles dispersed in the microstructure.

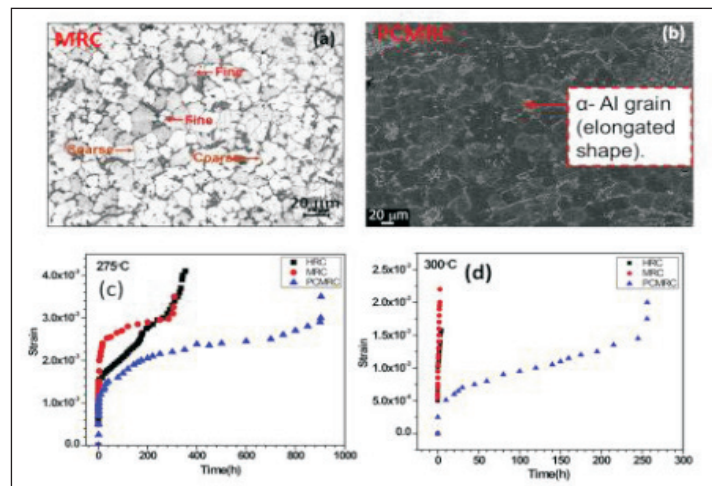


**Fig. 1 : Optical images showing the effect of mushy state rolling on microstructure: (a) mushy state rolled composite (MRC); (b) Pre-cold rolled mushy state rolled composite (PCMRC); as well as creep properties: (c) plots of creep strain against time for tests carried out at 275 °C; and (d) plots of creep strain against time for tests carried out at 300 °C [4,5].**

The plot of creep rate against  $\alpha - \alpha_0$  shows  $n$  in the range of 4-5 (Fig. 2(e). Additionally, the threshold stress has been found to decrease with increasing temperature. The appearance of the steady-state stage in the tertiary portion of the creep curves is ascribed to the formation of secondary  $M_{23}C_6$  precipitates during creep test at 750 and 800 °C. As shown in Fig. 2(f), interaction of dislocations with secondary  $M_{23}C_6$  precipitates is responsible for strengthening during the steady stage of tertiary creep.

### 2.2.2. Creep behaviour of a single crystal Ni-based superalloy

The single crystal Ni-based superalloy (DMS4M) containing Cr, Co, W, Re, Ta, Hf, Nb and Al, as developed at DMRL Hyderabad, shows a microstructure containing coherent  $\gamma'$  precipitates with cube-on-cube orientation relations being dispersed in the  $\gamma$  matrix (Fig. 3(a)) [7]. The creep curves have exhibited the predominance of tertiary stage, and the creep resistance observed for the crystals with stress axis along  $\langle 100 \rangle$  have been found to be much superior compared to those having  $\langle 110 \rangle$  orientations, as shown in Fig. 3(b). Based on the plots of stress against the Larson-Miller parameter, the DMS4M alloy has

creep resistance comparable with or superior to those of other second or third generation single crystal alloys including CMSX-4, Rene N5, CMSX-10, and Rene N6, as shown in Fig. 3(c). The raft formation has been found as the primary damage mechanism during creep. Additionally, the coarsening with growth of rafts has been found to be along normal to stress axis for creep with stress axis along  $\langle 100 \rangle$  (Fig. 3(d)), and at 45 ° for stress axis along  $\langle 110 \rangle$  (Fig. 3(e)), indicating that the preferred direction of coarsening of the  $\gamma'$  precipitates is  $\langle 100 \rangle$ . The raft thickness has been found to decrease with increasing applied stress, as shown in Fig. 3(f).

### 2.3 Development of Mo and Nb silicide-based alloys for use beyond Ni-based superalloys

The class of refractory-silicide based intermetallic alloys most widely studied are based on Mo and Nb-silicides, which have occupied a major focus of my research for the last three decades.

#### 2.3.1 Structure-property relations of Mo-Si-B alloys

##### 2.3.1.1 Microstructure and mechanical properties

The Mo-Si binary equilibrium phase diagram shows the existence of  $Mo_3Si$  with cubic (A15

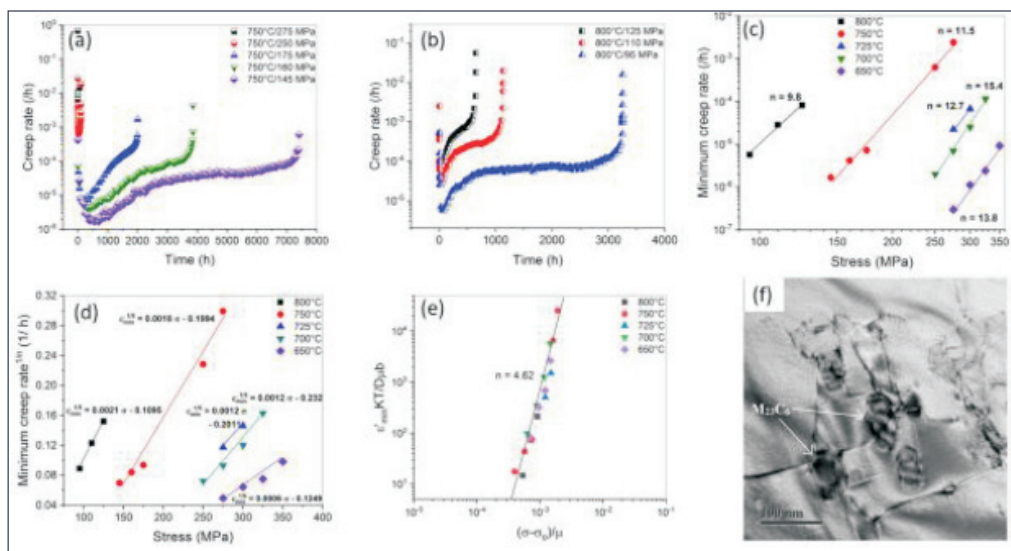


**Fig. 2 :** Results of creep tests on the IN617 alloy: the plots of creep rate against time for creep tests carried out at (a) 750 °C, and (b) 800 °C; (c) log-log plots of minimum creep rate against stress ( $\alpha$ ) with best-fit lines to find apparent stress exponent ( $n$ ); (d) plots of  $(\text{min. creep rate})^{1/n}$  against stress to find threshold stress ( $\alpha_0$ ); (e) plot of temperature-compensated creep rate against  $(\alpha - \alpha_0)$  to find true value of  $n$ , and (f) TEM image showing interaction of dislocations with  $M_{23}C_6$  particles during creep test at 800 °C under an applied stress of 125 MPa.

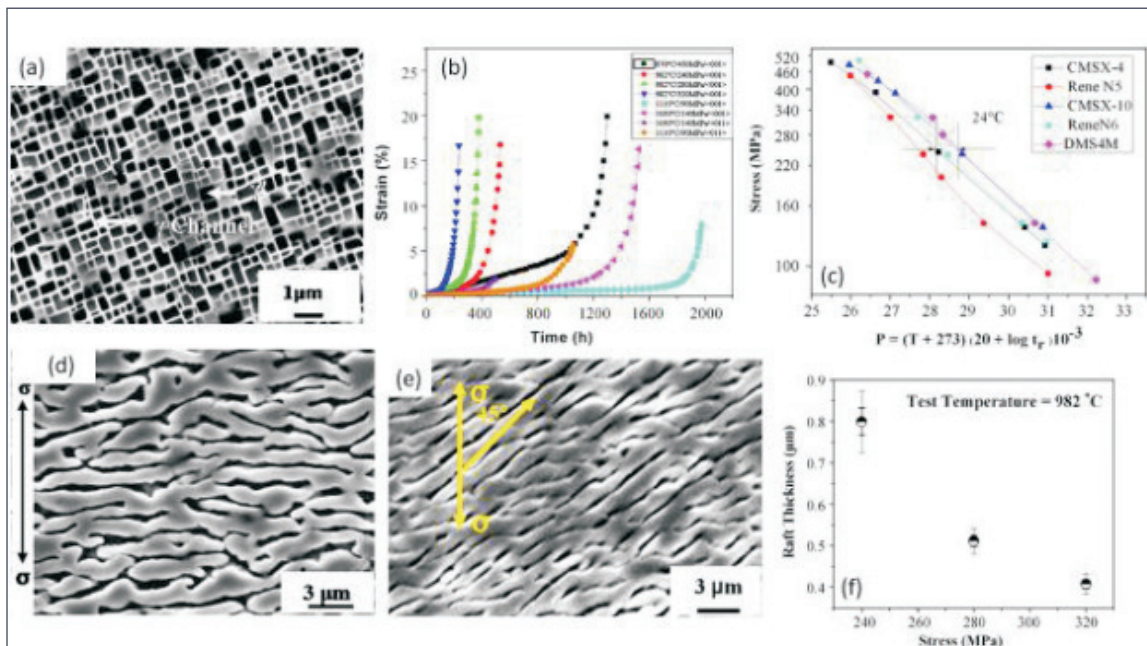


**Fig. 3 : Microstructure and creep behaviour of DMS4M single crystal Ni-based superalloy [7]: (a) SEM image depicting the microstructure showing cuboidal  $\gamma'$  precipitates; (b) plots of creep strain against time showing the predominance of tertiary creep; (c) plots of stress against the Larson-Miller parameter with the results obtained for other alloys of similar nature; SEM images indicating growth of rafts in a direction (d) perpendicular to stress axis for loading along  $\langle 100 \rangle$  direction, and (e) at  $45^\circ$  to the stress axis (i.e. along  $\langle 100 \rangle$ ) for loading along  $\langle 110 \rangle$ ; as well as (f) plot showing decrease of raft thickness with increase in stress.**

(strukturbericht), cP8 (Pearson symbol structure) structure, as well as  $\text{Mo}_5\text{Si}_3$  ( $D8_m$ , tI32) and  $\text{MoSi}_2$  (C11b, tI6) with tetragonal structure (Fig. 4) [8,9]. The melting points of  $\text{Mo}_3\text{Si}$ ,  $\text{Mo}_5\text{Si}_3$  and  $\text{MoSi}_2$  are  $2025^\circ\text{C}$ ,  $2180^\circ\text{C}$ , and  $2020^\circ\text{C}$ , respectively. Due to the complex crystal structure with low symmetry, the number of slip systems is less than 5, and the Peierls stress is high in the aforementioned Mo-silicides, which is responsible for their intrinsic brittleness, high brittle to ductile transition temperature ( $\geq 1100^\circ\text{C}$ ), as well as low fracture toughness ( $2\text{-}4\text{ MPa}\sqrt{\text{m}}$ ). Still, a significant attention has been paid to develop  $\text{MoSi}_2$  as a high temperature structural material, because of its superior oxidation resistance till  $1700^\circ\text{C}$  due to the formation of a continuous, stable and protective scale of  $\text{SiO}_2$ . By addition of ceramic reinforcement like  $\text{SiC}$  or  $\text{Al}_2\text{O}_3$  to  $\text{MoSi}_2$ , a marginal increase in fracture toughness is observed, as the crack paths become more tortuous due to crack deflection, crack bridging (Fig.5(a)). Additionally, the yield strength decreases sharply with increasing temperature, as shown in Fig. 5(b) [10,11].

Keeping the aforementioned limitations of the addition of ceramic reinforcement in mind, an approach involving the development of Mo-Si-B alloys leading to the formation of Moss (Mo-rich solid solution),  $\text{Mo}_3\text{Si}$  and  $\text{Mo}_5\text{SiB}_2$  as the constituent phases as predicted by the ternary equilibrium isotherm for  $1600^\circ\text{C}$  in Fig. 6(a) [12], has been pursued since the late 1990s [8,13]. Such an approach was triggered by the finding that the  $\text{Mo}_5\text{Si}_3$  with 2 wt% B and  $\text{Mo}_5\text{SiB}_2$  possess superior oxidation resistance due to the formation of a protective scale of borosilicate glass [14]. Additionally, the creep resistance of  $\text{Mo}_5\text{SiB}_2$  single crystal has been found to be greater than that of  $\text{MoSi}_2$  by three times [15]. In the Mo-Si-B system, the Moss being a ductile phase increases the fracture toughness, whereas  $\text{Mo}_3\text{Si}$  and  $\text{Mo}_5\text{SiB}_2$  contribute to the retention of high temperature strength along with the formation of a protective scale comprising borosilicate glass. The composition of 76Mo-14Si-10B has been chosen for study in my research group, considering an optimum amount

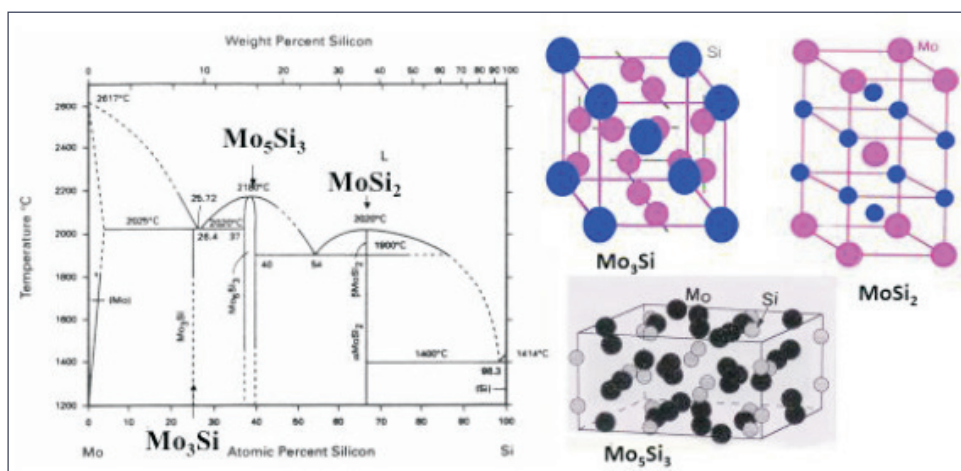


**Fig. 4 :** The Mo-Si binary equilibrium phase diagram showing the composition and melting points of the intermetallics, as well as schematic illustration of the crystal structures of  $\text{Mo}_3\text{Si}$  (A15),  $\text{Mo}_5\text{Si}_3$  (D88) and  $\text{MoSi}_2$  (C11b) [8,9].

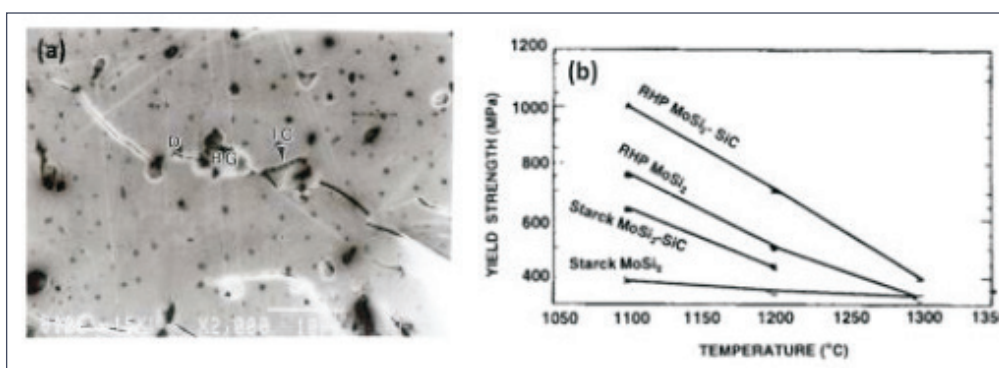


**Fig. 5 :** (a) Deflection and bridging of crack originating from indentation corner in  $\text{MoSi}_2$ -5.5Al alloy containing  $\text{Al}_2\text{O}_3$  particles [10]; (b) plots depicting the variation of yield strength with temperature [11].

of microstructural constituents. Typical load displacement plots obtained from the fracture toughness tests have shown non-linearity after the maximum load is reached (Fig. 6(b)), indicating the occurrence of non-catastrophic failure due to the arrest and bridging of crack by the ductile  $\text{Mo}_{ss}$  phase, see Fig. 6(c) [16]. The 76Mo-14Si-10B alloy has shown a modest fracture toughness of  $5 \text{ MPa}\sqrt{\text{m}}$ , but significantly higher yield strength compared to  $\text{MoSi}_2$  and  $\text{MoSi}_2$ -SiC composites in the temperature range of 1000-1350 °C, as shown in Fig. 6(d) [17].

### 2.3.1.2 Oxidation behaviour

On isothermal exposure of the 76Mo-14Si-10Nb alloy at temperatures in the range of 800-1300 °C, an initial mass loss followed by a regime of reduced or negligible mass change has been observed, whereas almost continuous mass loss

has been noticed at 700 °C [18]. The oxidation resistance is ensured by the formation of an oxide scale having the borosilicate glass as its outermost layer, which completely arrests the mass loss, as shown in Fig. 8(a). Studies involving short duration isothermal oxidation experiments at 1150 °C from 20 s onwards have shown that the surface of this alloy to be covered completely with the borosilicate glass (BSG) within 480 s, provides complete protection against further degradation, as shown in Fig. 8(b) [19]. As the  $\text{MoO}_3$  formed by the oxidation of the  $\text{Mo}_{ss}$  phase vaporizes, cavities are left behind, which are filled by the viscoplastic flow of BSG formed by oxidation of the surrounding  $\text{Mo}_3\text{Si}$   $\text{Mo}_5\text{Si}_3$  phases. The viscoplastic flow of the BSG during isothermal exposure at 1150 °C could be confirmed from the formation of ripples in the oxide scale, as shown in Fig. 8(c).

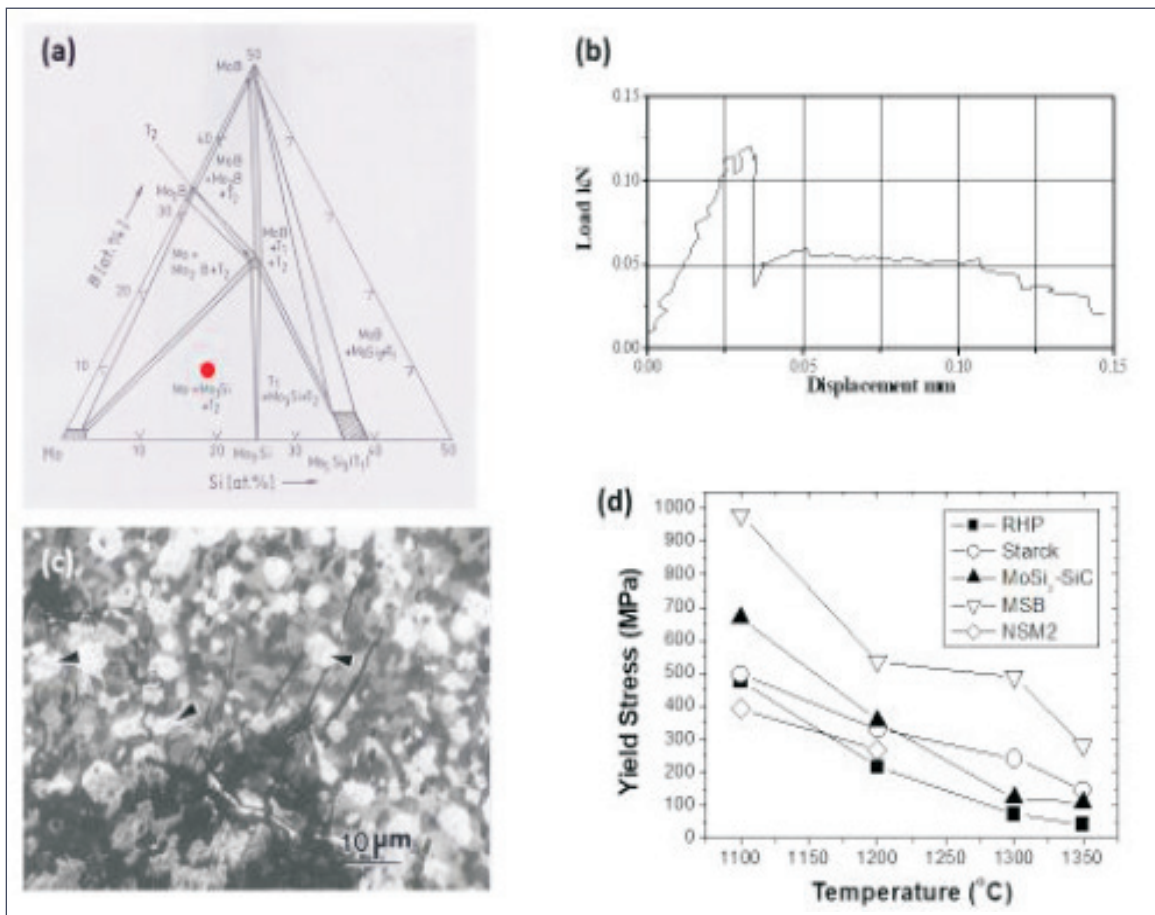


Fig. 6 : (a) Mo-rich part of the Mo-Si-B ternary phase diagram for 1600 °C [8,12]; (b) a typical load-displacement plot obtained from fracture toughness test on 76Mo-14Si-10B alloy [16], (c) path of indentation crack in 76Mo-14Si-10B alloy indicating bridging by ductile MoSi phase (arrowed) [14]; and (d) plots depicting the variation of yield strength with temperature for 76Mo-14Si-10B (MSB) alloy [17]. For comparison, the data obtained for reaction hot-pressed (RHP) MoSi<sub>2</sub>, hot-pressed MoSi<sub>2</sub> using powder from H.C. Starck, Germany (Starck), MoSi<sub>2</sub>-20 vol% SiC composite (MoSi<sub>2</sub>-SiC), as well as 76Nb-19Si-5Mo (NSM2) are plotted as well.

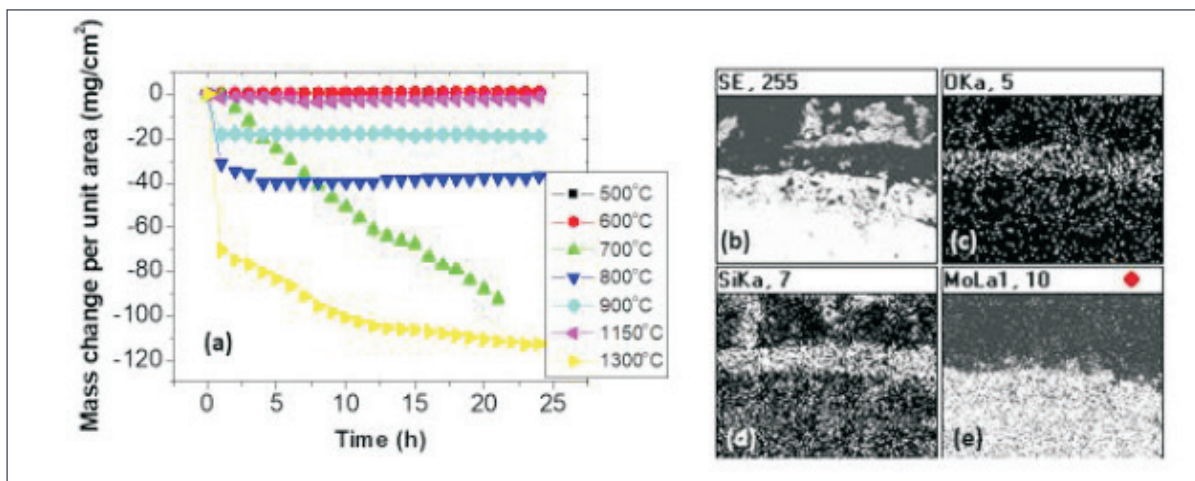
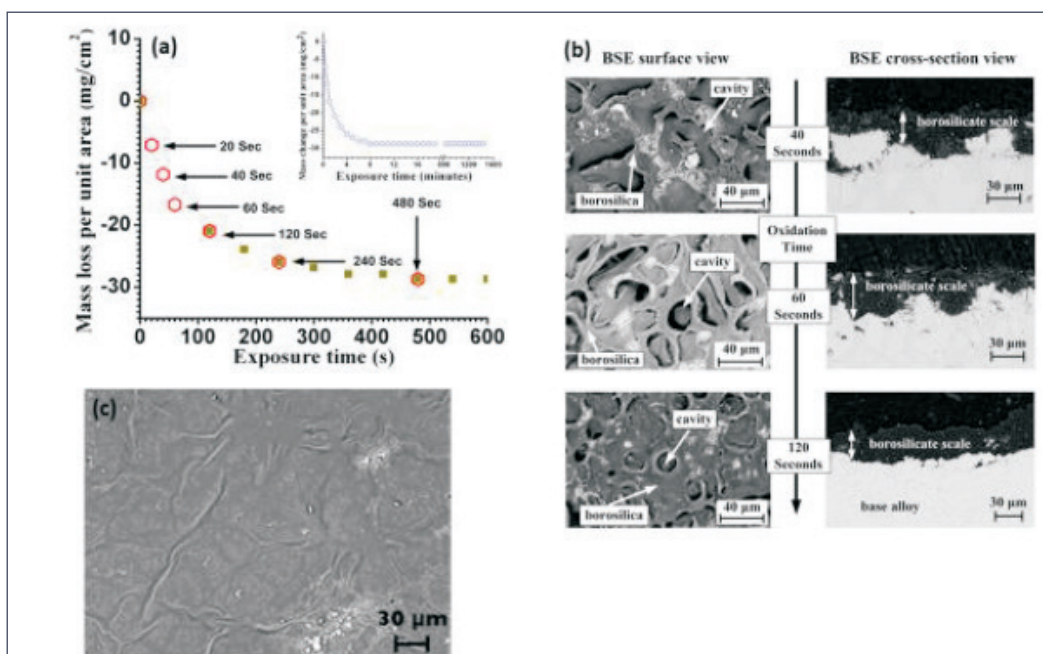


Fig. 7 : (a) Plots of mass change against time obtained from isothermal oxidation tests carried out in the range of 500-1300 °C on the 76Mo-14Si-10B alloy [18]; (b) SEM (BSE) image of the oxide scale along with EDS X-ray maps of (c) O, (d) Si and (e) Mo.



**Fig. 8 : Initial stages of exposure of the 76Mo-14Si-10B alloy at 1150 °C: (a) Plot of mass loss per unit area against time of exposure with inset showing the data recorded for 24 h; as well as SEM images showing (b) the top surfaces and oxide scale cross-section showing the cavities formed by oxidation of Moss phase with formation and escape of MoO<sub>3</sub> (g), along with filling up of the cavities by the flow of surrounding borosilicate glass formed by oxidation of Mo<sub>3</sub>Si and Mo<sub>5</sub>SiB<sub>2</sub>; (c) ripples formed by viscoplastic flow of the borosilicate glass during isothermal exposure [19].**

Experiments with addition of 2 at% Zr at the expense of Mo to the aforementioned alloy as well as processing by spark-plasma sintering instead of arc-melting have shown a significant refinement of grain size (Fig. 9) along with a noticeable decrease in the net mass loss (Fig. 10) [20]. Such an observation is justified partly due to the refinement of grain size, which by increasing the grain boundary and interfacial area fraction provides rapid diffusion paths for Si and B to the surface, leading to the formation of a protective scale. Additionally, the Zr acts as a glass-network modifier, and restricts devitrification. Further, the rapid consumption of MoO<sub>3</sub> to form the Zr(MoO<sub>4</sub>)<sub>2</sub> arrests the mass loss by its vaporization, whereas the formation of ZrSiO<sub>4</sub> lowers the amount of ZrO<sub>2</sub> in the oxide scale, and thereby limit the damage caused by the stresses generated owing to its phase transition. During exposure in moist air in the temperature range of 1000-1300 °C, greater mass loss compared to that in dry air along with the formation of cavities is found in the oxide scales due to vaporization of hydrated

MoO<sub>3</sub> and SiO<sub>2</sub>. However, formation of Zr(MoO<sub>4</sub>)<sub>2</sub> and ZrSiO<sub>4</sub> (Fig. 10(f)) along with strengthening of the glass network in the BSG and inhibition of devitrification in the oxide scales of the Zr containing alloys, are considered to have lowered mass loss by vaporization of hydrated MoO<sub>3</sub> and SiO<sub>2</sub>, as well as the formation of cavities [21].

### 2.3.2 Structure-Property relations of Nb-silicide based alloys

#### 2.3.2.1 Nb-Si-Mo alloys

The Nb-Si binary equilibrium phase diagram contains the intermetallics, Nb<sub>3</sub>Si, Nb<sub>5</sub>Si<sub>3</sub> and NbSi<sub>2</sub>, along with a eutectic at 17.5 at% Si (Fig. 11(a)) [22]. A considerable attention has been paid to the Nb-rich binary, ternary and multicomponent alloys with their microstructures being constituted by a mixture of Nb<sub>ss</sub> and 5-3 silicide (based on Nb<sub>5</sub>Si<sub>3</sub>). In the present study, Mo has been preferred as the ternary alloying element, because it is known to (i) form an isomorphous solid solution with Nb; (ii) make the diffusion kinetics sluggish; (iii) inhibit the

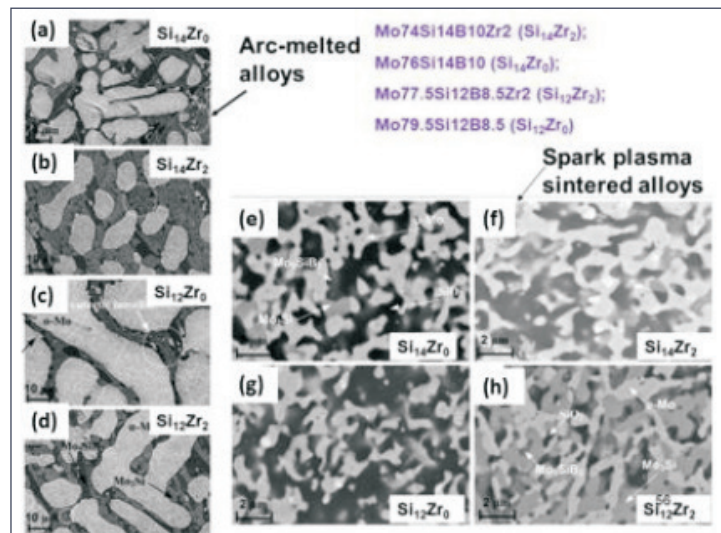


Fig. 9 : SEM images depicting the microstructures of (a-d) arc-melted and (e-h) spark plasma sintered Mo-Si-B and Mo-Si-B-Zr alloys [20].

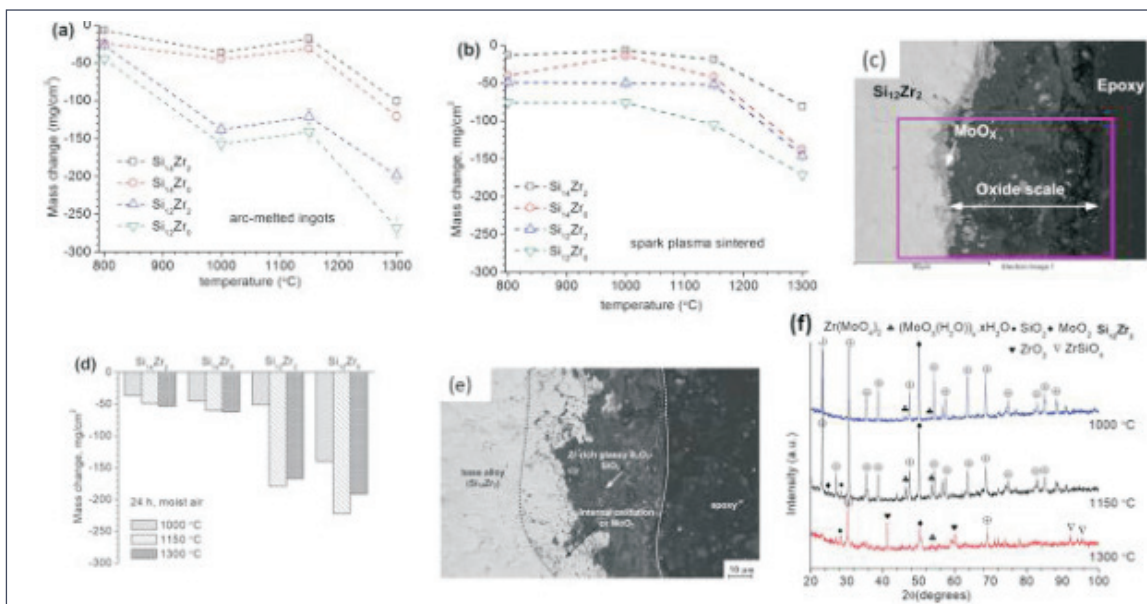


Fig. 10 : Plots of mass change with temperature on isothermal exposure for 24 h in dry air at temperatures between 800 °C and 1300 °C for (a) arc-melted and (b) spark plasma sintered Mo-Si-B and Mo-Si-B-Zr alloys; (c) cross-section of the oxide scale formed at 1000 °C; (d) bar-charts showing mass change on exposure in moist air at temperatures between 1000 °C and 1300 °C; (e) SEM image depicting the cross-section of the oxide scale formed in moist air at 1300 °C; and (f) XRD patterns from oxide scales formed in moist air [21].

formation of  $Nb_3Si$  as an additional brittle phase [23]; and (iv) stabilize the 5-3 silicide phase [24]. The microstructures contain a eutectic mixture of Nbss and 5-3 silicide phase, along with Nbss or 5-3 silicide as the primary phase in the alloys having hypo-eutectic or hyper-eutectic compositions, respectively [25]. Besides the well-expected lamellar morphology, a part of the eutectic colonies in the Nb-Si-Mo alloys also appears non-

lamellar and coarse due to the decoupled growth of  $Nb_{ss}$  and 5-3 silicide during solidification, being facilitated by large undercooling and complex crystal structure of the 5-3 silicide phase. The non-lamellar eutectic is found to be more effective in arresting and bridging of cracks, which contribute to toughening (Fig. 11(b)) [26]. The compression tests carried out at the strain rate of  $10^{-4}s^{-1}$  on hypoeutectic and hypereutectic alloys at

room temperature and 1200 °C (Fig. 11(c)) have led to the following inferences [27]: (i) the hyper-eutectic alloys have higher strength; (ii) the Mo-content has little influence on the compressive strength of the hyper-eutectic alloys; and (iii) the compressive strength of hypo-eutectic alloys scales with the Mo-content indicating the role played by its solid solution strengthening of the Nb<sub>ss</sub> phase. The oxidation kinetics at 1000 °C has been found to follow a parabolic rate law (Fig. 11(d)), with the mass gain being lower for the alloys with hyper-eutectic compositions, and further reduced with increase in the Mo-content [28]. In the oxide scale of the alloy with higher Mo-content (15 at%), formation of a continuous layer of SiO<sub>2</sub> at the alloy-oxide interface is considered to have contributed to the formation of a protective scale (Fig. 11(e)).

### 2.3.2.2 Effect of 20 at% Ti addition to Nb-Si-Mo alloys

On addition of 20 at% Ti to Nb-12Si-5Mo and

Nb-19Si-5Mo alloys, the following changes have been observed in the microstructure (Fig. 12): (i) formation of  $\beta\text{-Ti}_{ss}$  with Nb in solid solution, and (ii) increase in the amount of eutectic with non-lamellar morphology in comparison to lamellar eutectic [29, 30]. Additionally, annealing at 1500 °C for 100 h has led to the complete transformation of the eutectic from lamellar to non-lamellar morphology. The fracture toughness values obtained for the hypo-eutectic alloys with the ductile Nb<sub>ss</sub> as the primary phase have been found to be greater than those of the corresponding hyper-eutectic alloys (Fig. 13(a)) [31]. A significant increase in fracture toughness by 75% and 63% has been observed, respectively on addition of 20 at% Ti and annealing, with the observed maximum value of fracture toughness being  $\sim 14 \text{ MPa}\sqrt{\text{m}}$ . The observed increase in fracture toughness is considered to be due to the deviation of crack path from mode I propagation at the Nb<sub>ss</sub>/5-3 silicide interface (Fig. 13(b-d)).

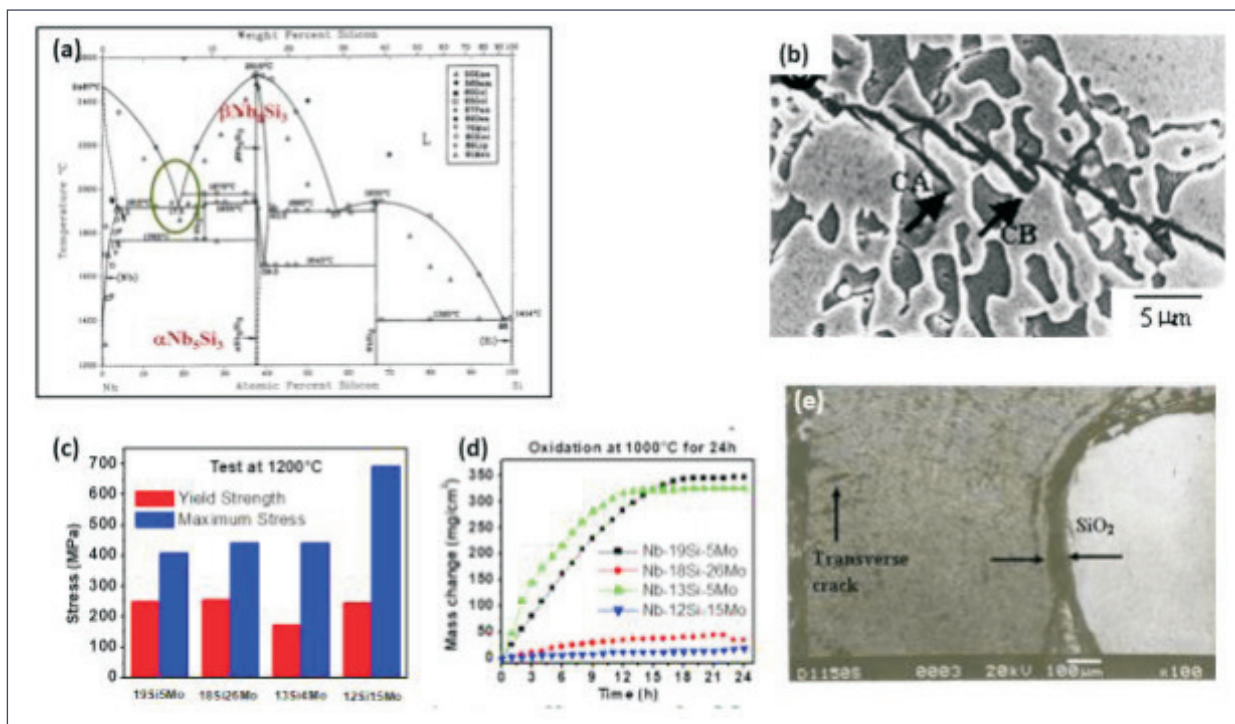


**Fig. 11 :** (a) Binary equilibrium phase diagram of the Nb-Si system showing the positions of intermetallics [22]; (b) path of indentation crack through the non-lamellar eutectic in the Nb-13Si-4Mo alloy [26]; (c) Bar charts showing yield strength and maximum stress obtained by compression tests at 1200 °C on hypoeutectic and hypereutectic Nb-Si-Mo alloys [27]; (d) Plots depicting the variation of mass change with duration of isothermal exposure at 1000 °C [28]; and (e) SEM image depicting the formation of a continuous and protective SiO<sub>2</sub> layer at the alloy-oxide interface in the cross-section of the oxide scale formed at 1000 °C on the Nb-18Si-26Mo alloy [28].

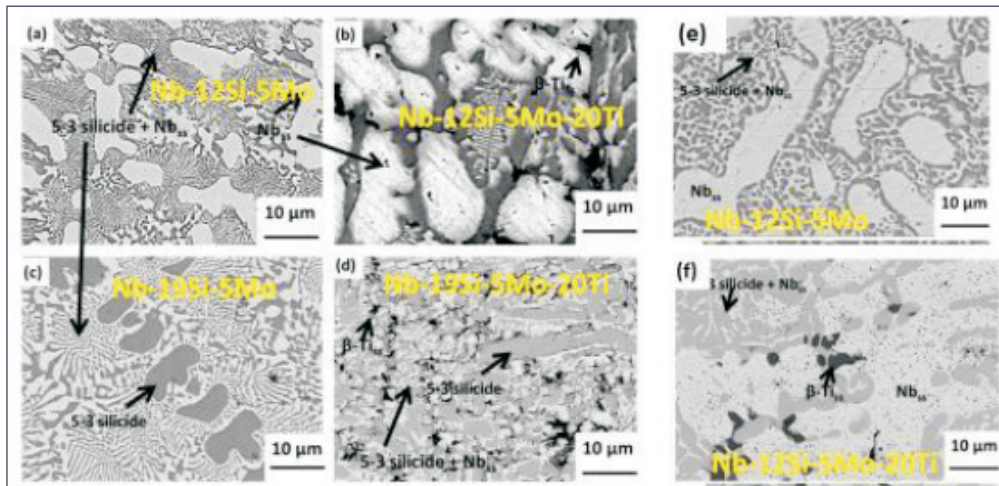


**Fig. 12 :** SEM (BSE) images depicting the microstructures of the arc-melted alloys with compositions: (a) Nb-12Si-5Mo, (b) Nb-12Si-5Mo-20Ti, (c) Nb-19Si-5Mo, (d) Nb-19Si-5Mo-20Ti, as well as post-anneal (1500 °C for 100 h) microstructures of the alloys: (e) Nb-12Si-5Mo, and (f) Nb-12Si-5Mo-20Ti [29, 30].

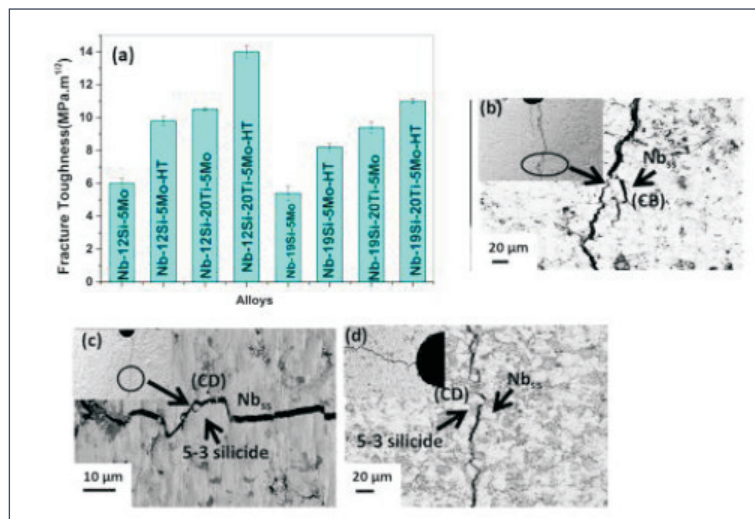


**Fig. 13 :** (a) Bar-charts depicting the fracture toughness of Nb-Si-Mo and Nb-Si-Mo-Ti alloys (HT indicates “annealed at 1500°C for 100 h); (b-d) SEM images of the crack profiles showing the interaction of the propagating crack with the microstructure [31].

The compression tests carried out at a strain rate of  $10^{-3} \text{ s}^{-1}$  between 900 °C and 1100 °C have shown that Ti addition does not affect the compressive strength significantly, with the exception of a modest increase being observed in the alloy with hypo-eutectic composition at temperatures  $\geq 1000 \text{ °C}$  (Fig. 14(a-b)) [32]. At a given temperature, the alloys with hypo-eutectic composition have been found to possess much superior strength retention ( $\alpha_{0.2}(T)/\alpha_{0.2}(RT)$ ) as a fraction of the yield strength at room temperature, being promoted by solid solution strengthening of the  $\text{Nb}_{ss}$  by Mo or Mo+Ti (Fig. 14(c-d)). The

addition of Ti has been found to have led to improved high temperature strength retention, with the contribution being most strongly noticed for the hypo-eutectic composition at 1100 °C.

Non-isothermal oxidation tests by heating up to 1300 °C and isothermal oxidation tests carried out in the range of 900-1200 °C (Fig. 15(a)) have shown lower mass gain for the Ti-containing alloys, compared to that observed in the corresponding hypo-eutectic or hyper-eutectic ternary Nb-Si-Mo alloy [32]. Additionally, the alloys with hyper-eutectic composition have exhibited superior oxidation resistance compared to the

corresponding hypo-eutectic alloys. The products of oxidation include  $\text{Nb}_2\text{O}_5$  and  $\text{SiO}_2$ , with  $\text{TiO}_2$ ,  $\text{TiNb}_2\text{O}_7$  and  $\text{Ti}_2\text{Nb}_{10}\text{O}_{29}$  being formed additionally in the oxide scales of the Nb-12Si-5Mo-20Ti and Nb-19Si-5Mo-20Ti alloys (Fig. 15(b)). Further, the thickness of oxide scales is found to be lower in case of the Ti-containing alloys having either hypo-eutectic or hyper-eutectic composition (Fig 15(c-d)). Analysis of the oxidation kinetics suggests an initial phase of interface-reaction controlled rapid increase of mass, followed by the stage of parabolic behavior, where diffusion of  $\text{O}^{2-}$  or  $\text{Ti}^{4+}$  through the oxide scale appears to be the rate-controlling in ternary or Ti-containing quaternary alloys, respectively. The formation of a relatively defect-free oxide scale, along with reduced oxygen solubility and diffusivity due to the presence of Mo and Ti in Nbss, along with formation of  $\text{SiO}_2$ -rich oxide on Nb-19Si-5Mo-20Ti alloy at 1100 °C and 1200 °C appears to be responsible for its superior oxidation resistance.

## 2.4 Development of ultra-high temperature ceramics

The ultra-high temperature ceramics based on  $\text{ZrB}_2$  and  $\text{HfB}_2$  have recently received major attention for use in leading edges and nose cones of hypersonic vehicles, because of their high melting points, moderate thermal and electrical conductivity, low coefficient of thermal expansion, and high chemical inertness in typically extreme environments. It has been reported in an earlier study that the oxidation of  $\text{ZrB}_2$  starts at  $\sim 800$  °C leading to the formation of a mixture of  $\text{ZrO}_2$  and  $\text{B}_2\text{O}_3$  (l) on the outermost surface as the oxidation products [33]. Since the  $\text{ZrO}_2$  is an anion-deficient semiconductor, the diffusion of oxygen anions through it is found to be very high [34]. The oxidation resistance of  $\text{ZrB}_2$  is significantly improved by reinforcing with SiC, which leads to the formation of a protective scale of borosilicate glass.

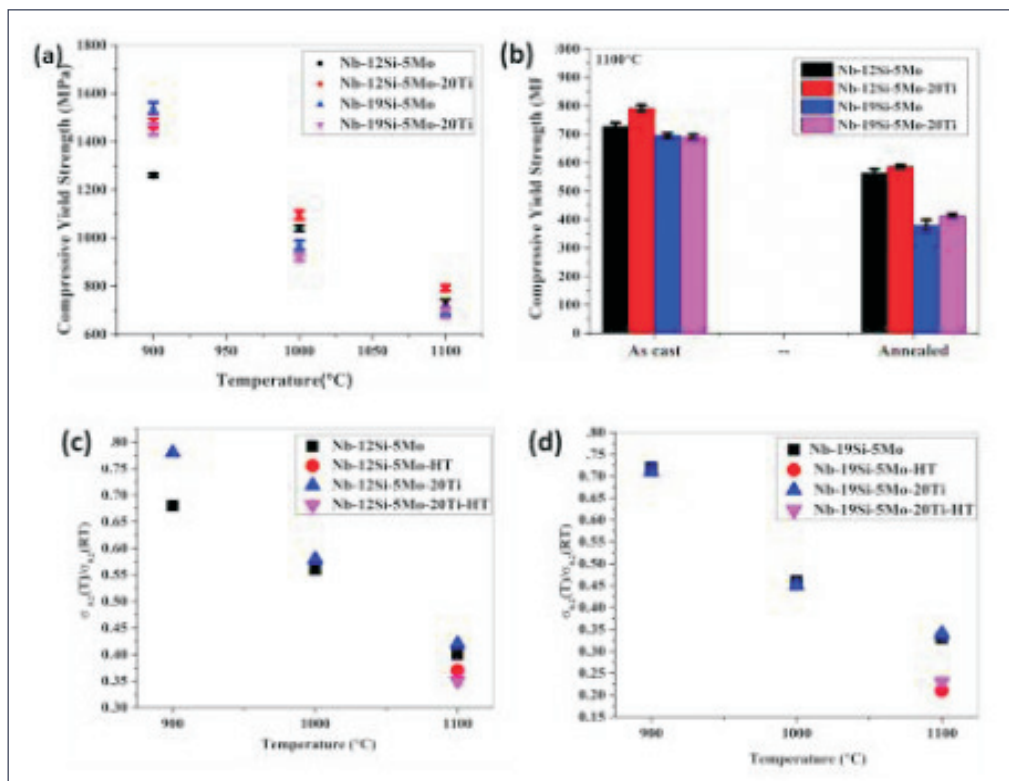


**Fig. 14 : Results of compression tests carried out at the strain rate of  $10^{-3} \text{ s}^{-1}$  on the Nb-Si-Mo and Nb-Si-Mo-Ti alloys [31]: (a) Plots depicting the variation of compressive yield strength with temperature, (b) Bar-charts depicting compressive yield strengths of arc-melted and annealed alloys; plots showing the variation of high-temperature strength-retention as function of temperature for (c) arc-melted and (d) annealed samples.**

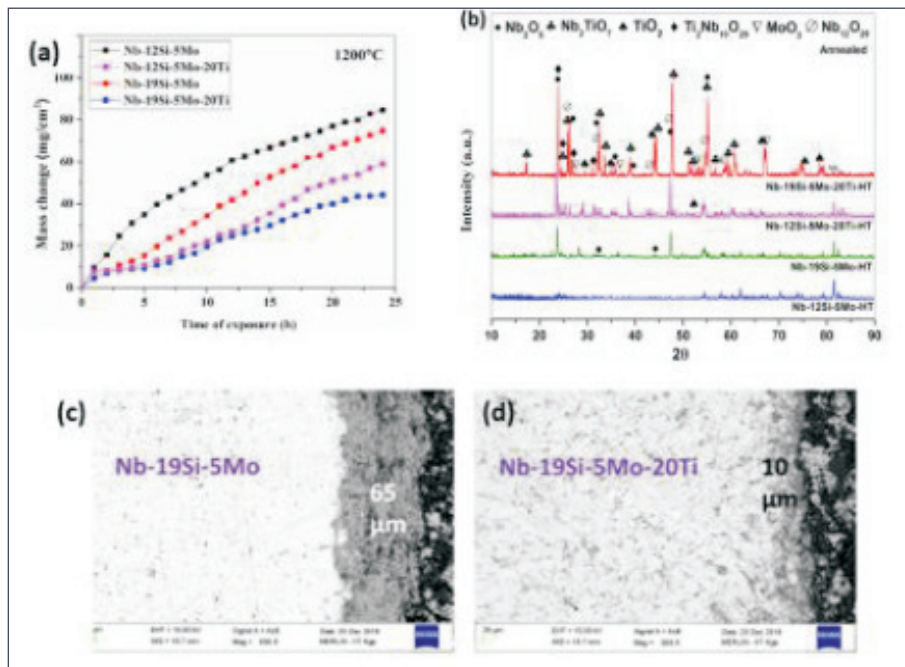


**Fig. 15 : Results of isothermal oxidation tests [32]: (a) Plots showing the variation of mass gain with temperature; (b) Typical XRD pattern from the oxide scale formed at 1100 °C as well as SEM images depicting the cross-sections of the oxide scales formed at 1100 °C on the alloys with compositions: (c) Nb-19Si-5Mo, and (d) Nb-19Si-5Mo-20Ti.**

The densification of  $ZrB_2$  is challenging due to low ionic diffusivity, presence of oxide impurities at powder particle surfaces, along with the requirement of high temperature for densification, which in turn leads to coarsening. Pressure-less sintering of  $ZrB_2$ -SiC composites has been found to lead to complete densification with the help of suitable additives. This process is considered promising for preparing near-net shaped composites, but needs to be optimized to maximize the amount of densification without grain coarsening, so that the desirable mechanical properties are achieved. On the other hand, hot pressing leads to near-theoretical density with impressive mechanical properties, but this process is suitable only for fabrication of simple shapes. Additionally, spark plasma sintering can be used for densification at relatively lower temperatures without grain coarsening.

#### 2.4.1. Pressure-less sintered $ZrB_2$ -SiC composites

A technique for pressure-less sintering of  $ZrB_2$ -SiC composites has been developed in our research group by using  $B_4C$  and C (added as 2 wt% phenolic resin) as additives [35]. In this process,

the composite mixture prepared by blending of powders and additives in a ball mill with WC-Co vials and balls, is cold compacted in a uniaxial press, and subsequently pressure-less sintered in argon environment. This process involves pre-sintering at 850 °C for 1 h to get rid of volatile constituents of phenolic resin such that only C is left behind. Thereafter, the powder mixture is subjected to intermediate holds at 1250 °C and 1600 °C for 0.5 h each for the surface oxides to be reduced by  $B_4C$  and C, and then finally sintered at 2000 °C for 1 h. The temperatures for intermediate hold have been chosen such that the free energies of the reactions leading to the reduction of  $SiO_2$ ,  $B_2O_3$  and  $ZrO_2$  by  $B_4C$  or C are negative [36]. Observation of the microstructures has shown a W-rich network at  $ZrB_2$  grain boundaries and  $ZrB_2$ -SiC interfaces (Fig. 16(a-b)). The W is considered to have been added to the powder mixture during ball-milling by erosion of WC-Co balls and vials by the abrasive SiC particles, which is supported by increase of W-concentration with SiC content. The formation of a continuous network along with the rounded corners of grains is considered to be the evidence for the formation of a liquid phase, which

appears to have helped densification. The relative density of the pressure-less sintered composites is found to rise with SiC content, and also increase significantly on subjecting to isothermal hold at 1250 °C and 1600 °C for 0.5 h (Fig. 16(c)) [35].

The thermal diffusivity of the investigated composites, measured by the laser-flash method, has been found to be the highest for the ZrB<sub>2</sub>-20 vol% SiC composite (Fig. 17(a)) [37]. Although the thermal conductivity of SiC is higher than that of ZrB<sub>2</sub>, reduction in grain size along with the increase in interfacial area with increase in

SiC volume fraction leads to enhanced phonon scattering, which in turn lowers the thermal conductivity for SiC content >20 vol%. Among the samples subjected to thermal shock by heating the to 800 °C, 1000 °C and 1200 °C followed by quenching in water has shown the least increase in indentation crack length as well as the lowest reduction of hardness for the ZrB<sub>2</sub>-20 vol% SiC composite (Fig. 17(b-c)). Such an observation indicating the lowest thermal-shock induced damage in the ZrB<sub>2</sub>-20 vol% SiC composite is ascribed to its thermal conductivity found to be the highest.

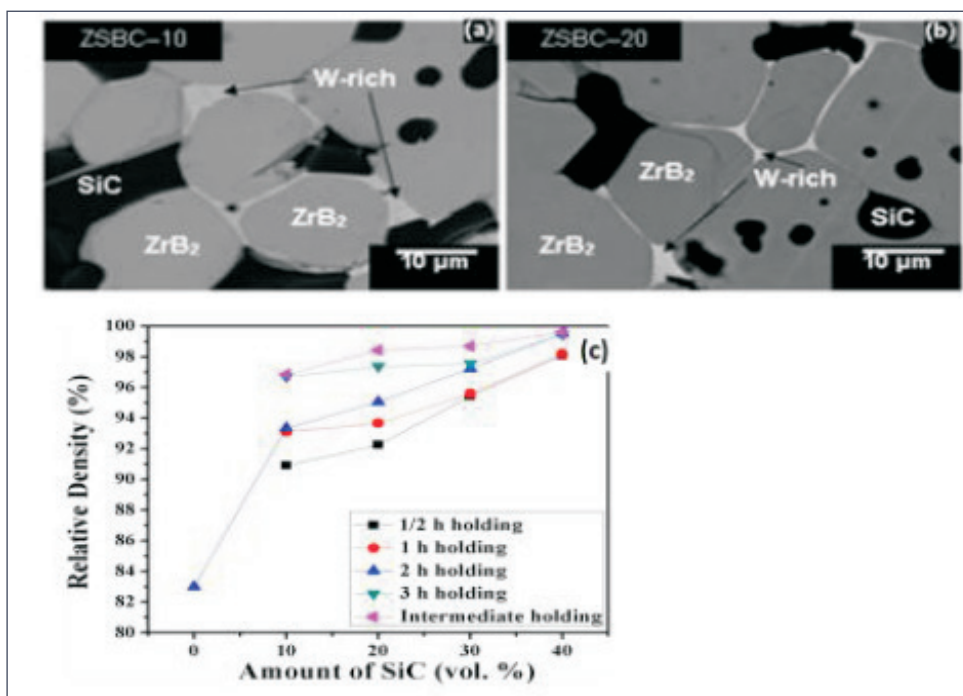


Fig. 16 : SEM (BSE) images depicting the microstructures of pressureless sintered ZrB<sub>2</sub>-SiC composites with SiC content of (a) 10 vol%, (b) 20 vol% (with W-rich phase at the interfaces), and (c) variation of relative density with SiC content for different sintering durations [35].

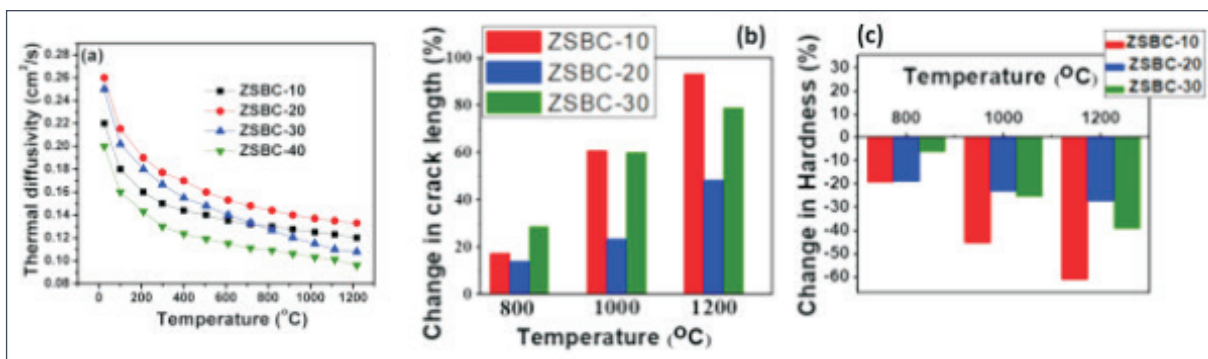


Fig. 17 : (a) Plots depicting the variation of thermal diffusivity with increasing temperature; bar charts showing changes in (b) indentation crack length and (c) hardness measured using Vickers hardness testing machine operated with 10 kgf load[37].

The samples subjected to ablation tests by exposing to oxy-acetylene (OA) flame have shown the average temperatures at front face and back face as  $\sim 2200$  °C and  $\sim 1600$  °C, respectively with variations of  $\pm 50$  °C [37]. The slope for rise of temperature has been found to be the sharpest in case of the ZrB<sub>2</sub>-20 vol.% SiC composite, probably because of its higher thermal conductivity. On exposure to the OA flame, the surfaces of composites with 10 or 30 vol% SiC appear to be rough with a network of pores with significantly large discontinuities, whereas the surface of the ZrB<sub>2</sub>-20 vol% SiC composite has been found to be smoother with finer pores (Fig. 18(a-f)). The EDS spectrum of the ablated surfaces (Fig. 18(g)) shows peaks of Zr, Si and O, indicating the formation of ZrO<sub>2</sub> and ZrSiO<sub>4</sub> and confirmed by the XRD analysis as well (Fig. 18(h)). As indicated by the ZrO<sub>2</sub>-SiO<sub>2</sub> phase diagram, ZrO<sub>2</sub> + liquid is formed at the OA flame temperature, which on solidification forms ZrO<sub>2</sub> + ZrSiO<sub>4</sub> [38]. The ZrO<sub>2</sub> acts as thermal insulation for the composite, whereas the liquid closes the surface pores. As is evident from the bar-charts depicting the changes in Young's modulus due to the ablation test (Fig. 18(i)), the ZrB<sub>2</sub>-20 vol% SiC composite has been found to be more resistant to damage

compared to that with 10 vol% SiC composite: this is probably due to the less amount of liquid formed at the flame temperature in case of the latter composite. Having higher than 20 vol% SiC is found to be detrimental probably because of the active oxidation of SiC to form SiO(g) becoming predominant. Formation of ZrSiO<sub>4</sub> lowers the formation of SiO (g). The amount of ZrSiO<sub>4</sub> is found to be maximum in the oxide scale of ZrB<sub>2</sub>-20 vol% SiC composite, because an optimum amount of ZrO<sub>2</sub> and SiO<sub>2</sub> is probably formed during high temperature exposure.

#### 2.4.2. Hot pressed ZrB<sub>2</sub>-SiC composite

Composites were hot-pressed in argon environment at 2000 °C under 30 MPa pressure for 30 min; they contained ZrB<sub>2</sub>-20 vol% SiC, ZrB<sub>2</sub>-20 vol% SiC-5 vol% Si<sub>3</sub>N<sub>4</sub>, and ZrB<sub>2</sub>-20 vol% ZrC-20 vol% SiC-5 vol% Si<sub>3</sub>N<sub>4</sub> [39]. A typical microstructure of the hot-pressed ZrB<sub>2</sub>-20 vol% SiC composite is shown in Fig. 19(a). Evaluation of the room-temperature mechanical properties of these composites has shown that the ZrB<sub>2</sub>-20 vol% SiC-5 vol% Si<sub>3</sub>N<sub>4</sub> composite possesses the highest hardness ( $\sim 21.2 \pm 2$  GPa), flexural strength ( $\sim 520 \pm 6$  MPa) and fracture toughness ( $\sim 7.8 \pm 0.6$  MPa $\sqrt{m}$ ) among the investigated

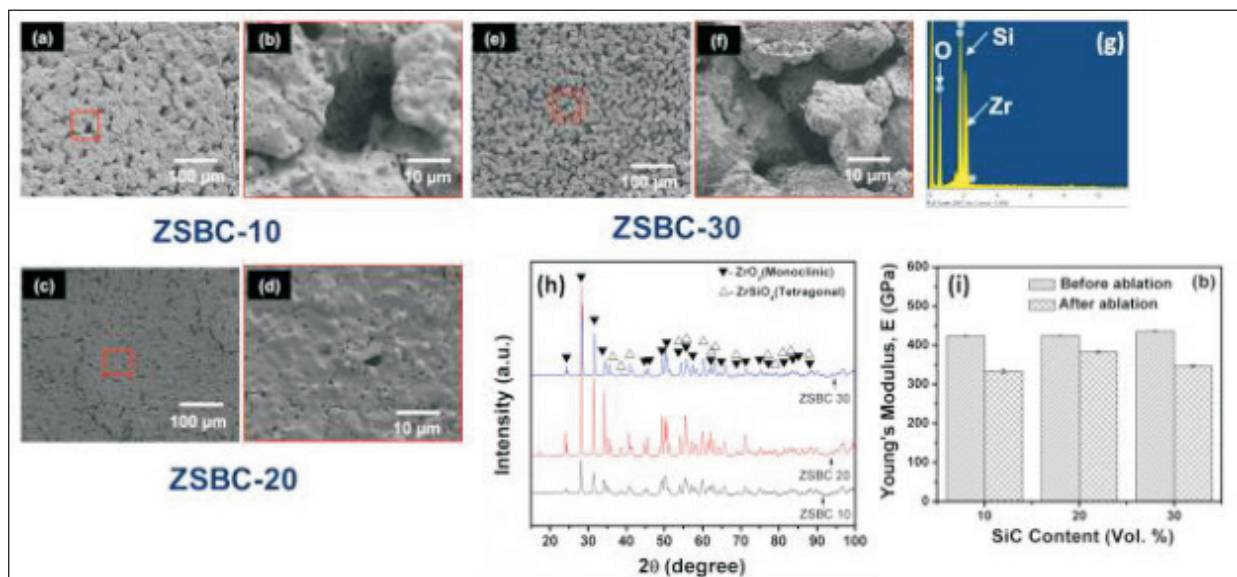


**Fig. 18 : Results of ablation tests [37]: SEM images depicting the top surfaces of the oxide scales formed as a result of ablation test on (a-b) ZrB<sub>2</sub>-20SiC-7LaB<sub>6</sub> (ZSBCL-7); (c-d) ZrB<sub>2</sub>-20SiC-10LaB<sub>6</sub> (ZSBCL-10); (e-f) ZrB<sub>2</sub>-20SiC-14LaB<sub>6</sub> (ZSBCL-14); (g) EDS spectrum from the oxide scale showing peaks of Zr, Si and O; as well as (h) XRD patterns from the oxide scales; and (i) bar charts depicting Young's modulus before and after ablation test.**

hot-pressed composites. The ZrB<sub>2</sub>-20 vol% SiC composite processed by hot pressing has been found to possess finer grain size and higher hardness compared to that obtained by pressure-less sintering.

The creep tests carried out in the range of 1300-1425 °C on ZrB<sub>2</sub>-20 vol% SiC (ZS) and ZrB<sub>2</sub>-20 vol% SiC-5Si<sub>3</sub>N<sub>4</sub> (ZSS) composites have consistently shown lower steady state strain rate in case of the former composite (Fig. 19(b)) [40]. The stress exponent (n) has been found to be between 1.1 and 1.7 for the ZS, and between 0.6 and 1.6 for the ZSS, with the values being <1 for temperatures ≥1400 °C (Fig. 19(b)). The obtained values of n are suggestive of diffusion-controlled creep. The activation energy has been found as ~95±32 kJ/mol at temperatures ≤1350 °C, which is close to that for diffusivity of O<sub>2</sub> through SiO<sub>2</sub>, as shown in Fig. 19(c) and (d). On the other hand, the activation energy at temperatures ≥1350 °C has been found as ~470±20 kJ/mol, which agrees with that required for the visco-plastic flow of

the intergranular glassy film. The values of n < 1 observed for the ZSS composite creep tested at ≥1400 °C is ascribed to the presence of Si<sub>3</sub>N<sub>4</sub> in its microstructure, which is known to undergo by grain boundary sliding accommodated by solution and reprecipitation. At high temperatures, the Si<sub>3</sub>N<sub>4</sub> dissolves in the Si-N-O glassy phase, followed by precipitation of the Si<sub>2</sub>N<sub>2</sub>O at the grain boundaries and particle-matrix interfaces. Additionally, the post-creep microstructures have shown cracks at ZrB<sub>2</sub> grain boundaries and ZrB<sub>2</sub>-SiC interfaces, along with voids at grain boundary triple points, which appear to have formed by grain boundary sliding, as shown in Fig. 19(e).

### 2.4.3. Composites processed by spark plasma sintering

#### 2.4.3.1 Processing

The ZrB<sub>2</sub>-20 vol% SiC composites with 7, 10 and 14 vol% LaB<sub>6</sub> (marked as ZSBCL7, ZSBCL10 and ZSBCL14, respectively) added at the expense of ZrB<sub>2</sub> along with B<sub>4</sub>C and C being present

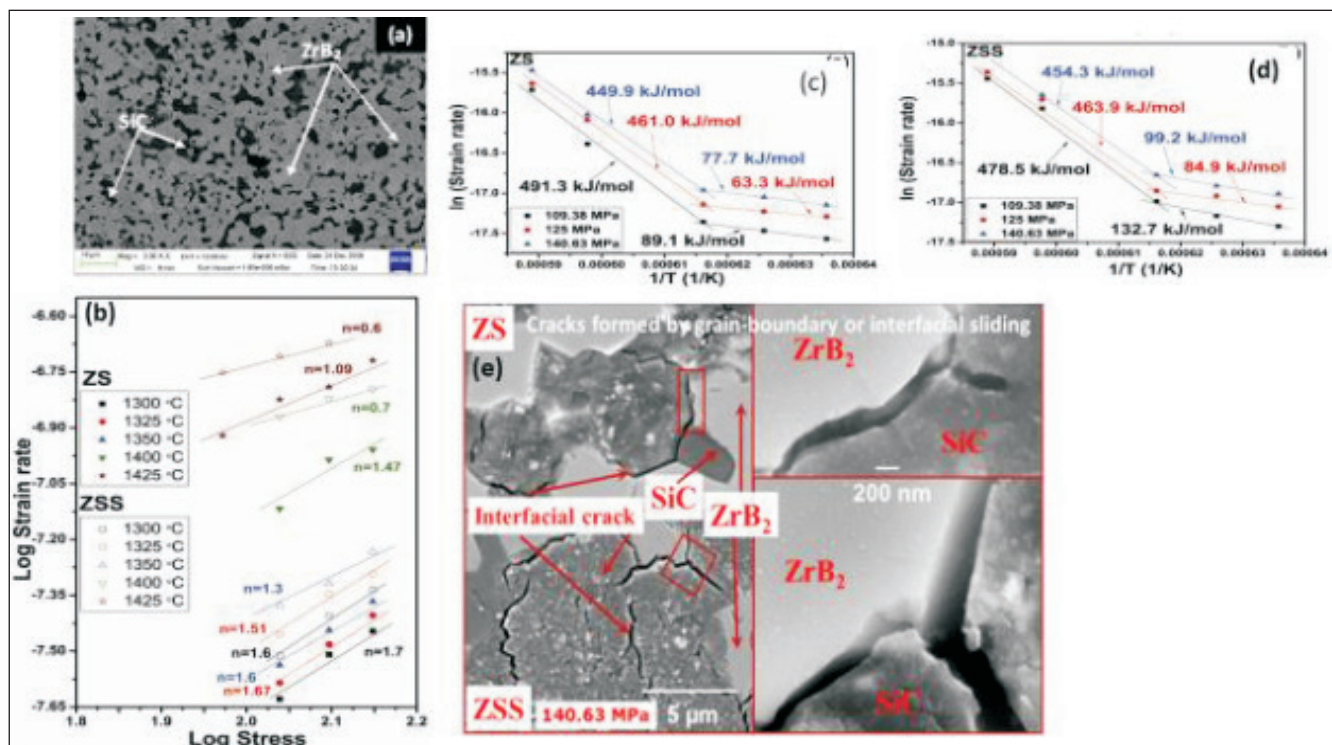


Fig. 19 : (a) SEM image showing the microstructure of the ZrB<sub>2</sub>-20 vol% SiC composite, (b) log-log plots of steady state creep strain rate with stress with best-fit lines drawn to find stress exponents (n), Plots of log creep strain rate against the reciprocal of absolute temperature to find activation energy for creep for the composites (c) ZrB<sub>2</sub>-20 SiC (ZS) and (d) ZrB<sub>2</sub>-20 SiC-5 Si<sub>3</sub>N<sub>4</sub> (ZSS), (e) SEM images showing evidence of cracking due sliding of grain boundaries and ZrB<sub>2</sub>-SiC interfaces during creep [40].

as additives, have been processed by spark plasma sintering at 1600 °C or 1800 °C in argon environment using ram pressure of 50 and 70 MPa, respectively [41]. For SPS at 1600 °C and 1800 °C, the samples were isothermally held at 1300 °C and 1500 °C, respectively for 2 min. In spite of higher temperature and pressure, the densification achieved is less at 1800 °C compared to that at 1600 °C. The spark-plasma sintering process can be divided into three zones (Fig. 20(a-b)). The first zone includes the stage of heating to the intermediate hold temperature, whereas in the second zone the temperature is raised to that of intermediate hold. In the third zone, soaking has been carried out at 1600 °C or 1800 °C for the maximum relative density to be achieved (Fig. 20(c)). The relative densities prior to soaking in the third zone are ~92-94% for SPS at 1600 °C, and ~84-89% for SPS at 1800°C. Based on the analysis of the ram displacement the densification rates at 1600 and 1800 °C have been calculated, and the creep occurring during soaking at 1600 °C and 1800 °C has been analysed to find stress exponents (n), 4.9-6.7 and 2-3.2, respectively, as shown in Fig. 20(d) and (e), respectively. Based on the values of n, the mechanism of creep is

identified as dislocation climb controlled for SPS at 1600 °C. On the other hand, the values of n for SPS at 1800 °C suggest the predominance of diffusion-controlled creep with grain boundary sliding in case of ZSBCL-7 and ZSBCL-10, but the operation of dislocation glide controlled creep for the ZSBCL-14. Arrays of dislocations (straight and curved) with some having jogs in the ZrB<sub>2</sub> grains can be considered as the evidence of dislocation creep (Fig. 20(f)). Lower densification during SPS at 1800 °C is ascribed to incomplete removal of impurity oxides along with higher rate of vaporization of B<sub>2</sub>O<sub>3</sub>, which leads to the retention of porosities.

#### 2.4.3.2 Oxidation behaviour

Non-isothermal oxidation experiments carried out by heating in a thermo-gravimetric analyser in air from room temperature to 1400 °C have shown the highest mass gain for the ZSBCL-14 composites, which is ascribed to rapid oxidation of the LaB<sub>6</sub> [42] However, isothermal and cyclic oxidation experiments for 24 h in the range of 1300-1500 °C have shown the least mass gain in case of the ZSBCL-14 composite, which is ascribed to the formation of a protective scale after exposure for a minimum duration of 8-10 h.

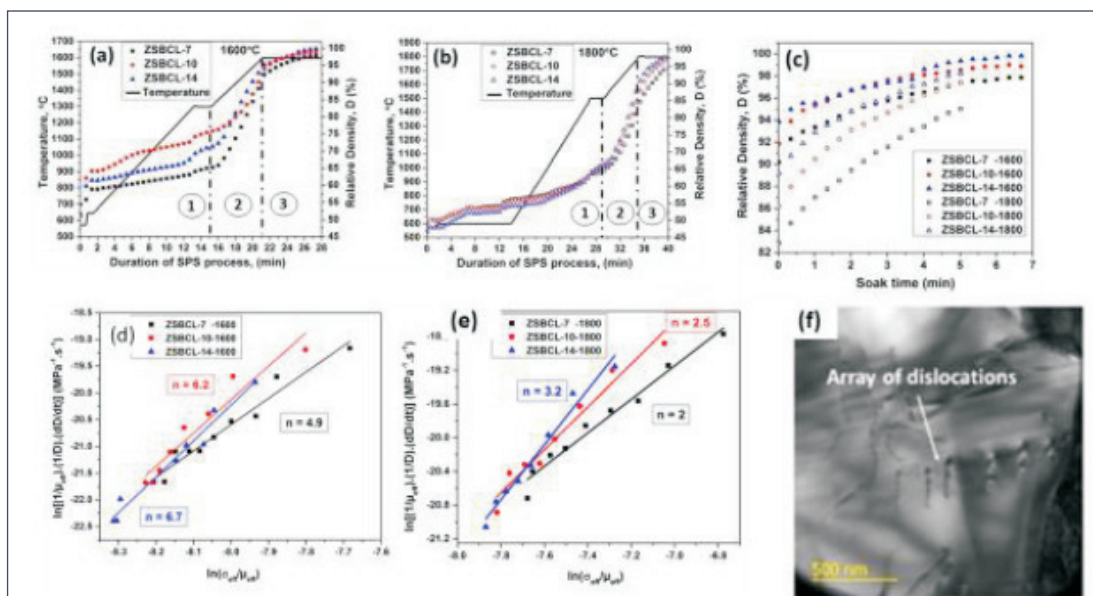


**Fig. 20 :** Plots depicting the variation of temperature for spark plasma sintering at (a) 1600 °C, and (b) 1800 °C; (c) plots showing the variation of relative density with duration of soaking; plots of densification rate with normalized stress for final soaking at (d) 1600 °C and (e) 1800 °C; (f) a TEM bright field image showing dislocation activity in the ZrB<sub>2</sub>-20 vol% SiC-10 LaB<sub>6</sub> composite [41]

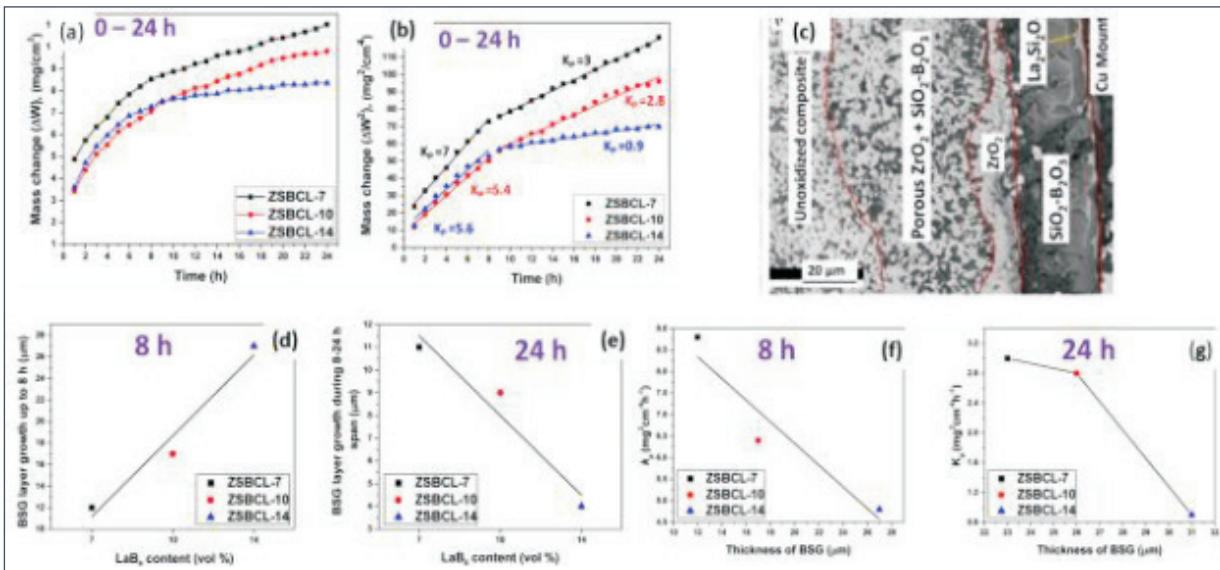


**Fig. 21 :** The results of oxidation tests at 1300 °C [43]: (a) plots of mass change with temperature during isothermal exposure at 1300 °C; (b) plots depicting the variation of (mass gain per unit area)<sup>2</sup> with time to find parabolic rate constant,  $k_p$ ; (c) SEM (BSE) image depicting the oxide scale cross-section formed after exposure for 24 h in the  $ZrB_2$ -20 SiC-14  $LaB_6$  composite; plots depicting the variation of borosilicate glass (BSG) layer growth rate with  $LaB_6$  content for durations up to (d) 8 h, and (e) 24 h; variation of  $k_p$  with thickness of BSG for durations up to (f) 8 h, and (g) 24 h.

On isothermal oxidation at 1300 °C, the change in mass gain with time follows a parabolic behaviour with a protective layer of BSG being developed right after the outermost layer of  $La_2Si_2O_7$  (Fig. 21(a-c)) [43]. The contribution of  $LaB_6$  to the oxide scale formation includes the formation of  $B_2O_3$  along with  $La_2O_3$ , which combines with  $SiO_2$  and oxygen at the outer surface to form  $La_2Si_2O_7$ . It should be also noted that the amount of  $B_2O_3$  formed by the oxidation of one of  $LaB_6$  is 3 times more than that produced by the oxidation of a mole of  $ZrB_2$ . Therefore, the growth rate of BSG is found to increase following a linear relation with the  $LaB_6$  content of the investigated composites during exposure up to 8 h, but decrease with  $LaB_6$  content during 8-24 h (Fig. 21(d-e)). For durations of both 0-8 h and 8-24 h, the parabolic rate constant,  $k_p$  has been found to decrease with the increasing  $LaB_6$  content, which can be considered as a confirmation of the critical role played by the BSG layer in protection against oxidation (Fig. 21(f-g)).

Isothermal exposure for 24 h at 1400 and 1500 °C has led to formation of oxide scales containing an outer layer of BSG with a thin film of  $La_2Si_2O_7$  on the top surface, which is followed by the layers

comprising coarse  $ZrO_2$ +BSG, fine  $ZrO_2$  + BSG, followed by a SiC depleted layer at the composite-oxide interface (Fig. 22) [42,44]. In the oxide scale of the composite isothermally exposed at 1500 °C, a mixed layer containing La-Zr-Si-B-O is present above the SiC depleted layer. The SiC depleted layer is believed to have been formed by the active oxidation of SiC, leading to the formation and escape of SiO (g) and CO (g). Higher active oxidation of SiC at 1500 °C than that at 1400 °C is also considered to be responsible for lower mass gain observed at the higher temperature. The BSG containing  $B_2O_3$  (l) formed at the oxide-composite interface by oxidation of  $ZrB_2$  and  $LaB_6$  is considered to have enough fluidity for moving outwardly by capillary action, filling up the pores thereby forming the outermost layer of the oxide scale. The formation of an inner layer enriched in La-Zr-Si-B-O within the oxide scale on exposure at 1500 °C indicates that  $ZrO_2$  and  $La_2O_3$  formed by oxidation of  $ZrB_2$  and  $LaB_6$ , respectively are partially dissolved in the BSG. Of course, its viscosity is increased by dissolution of  $ZrO_2$  and  $La_2O_3$ , along with stabilization of the glass network. The  $ZrO_2$  + BSG layer is expected to have formed by the precipitation of  $ZrO_2$  from the

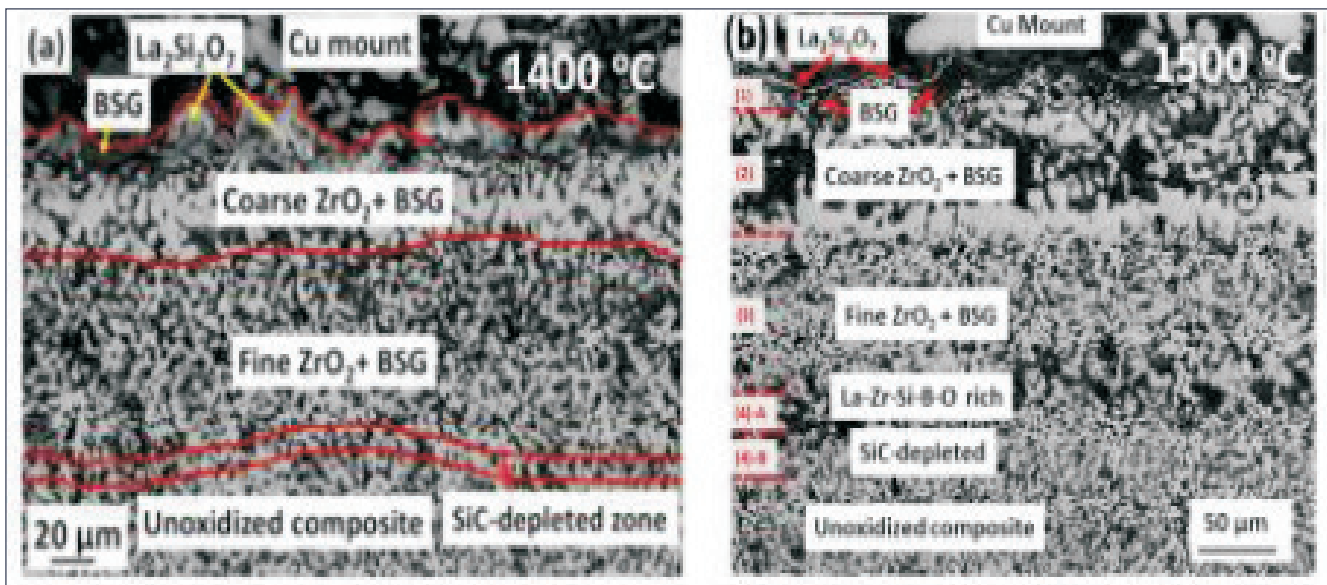


Fig. 22 : SEM (BSE) images showing various layers of oxide scales formed during isothermal exposure for 24 h at (a) 1400 °C and (b) 1500 °C [42, 44].

BSG. Additionally, the outermost layer of  $\text{La}_2\text{Si}_2\text{O}_7$  is also considered to have formed by precipitation from the BSG. The activation energy for oxidation obtained on the basis of the  $k_p$  values obtained by analyzing the isothermal exposure test data is found to be considerably greater than that of  $\text{O}_2$  required for diffusion through  $\text{SiO}_2$ , because of the complex nature of the BSG scale containing  $\text{ZrO}_2$  and  $\text{La}_2\text{O}_3$ , formed on the investigated composites.

Cyclic oxidation behaviour has been studied by subjecting 24 cycles of 1 h exposure (24 h) and 10 cycles of 10 h exposure (100 h) at 1400 °C [42]. The oxide scale formed by cyclic exposure has been found to contain an outer compact layer (OCL) comprising BSG+ $\text{ZrSiO}_4$  with a film of  $\text{La}_2\text{Si}_2\text{O}_7$  at the top surface, which is followed by an intermediate layer of  $\text{ZrO}_2$ +BSG, and thereafter a SiC-depleted zone located at the oxide-composite interface (Fig. 23(a)). After cyclic oxidation for 24 h, the mass gain is found to have the least value in the ZSBCL-10, whereas after 100 h of cyclic oxidation, the ZSBCL-14 is found to have gained the least mass, with ZSBCL-7 being the most prone to oxidation under either conditions of cyclic oxidation (Fig. 23(b-c)). The values of  $k_p$  are found to decrease linearly with increase in the thickness of the OCL in the oxide scales of the composites subjected to 10 cycles of 10 h each

at 1400 °C (Fig. 23(d)). This observation can be considered as a confirmation of the role of the OCL in protection against oxidation.

### 3. Concluding remarks and future directions

The research outcomes discussed in this lecture are summarized below:

- 1) Mushy state rolling with prior cold rolling has been found to significantly improve creep resistance of in-situ Al4.5Cu-5TiB<sub>2</sub> composite.
- 2) A steady state behaviour in tertiary creep stage of IN617 alloy caused by carbide precipitation slows creep damage at 750-800 °C.
- 3) Creep resistance of single Ni-based superalloy is much more along <100> than that along <110>. Coarsening of  $\gamma'$  is preferred along <100> irrespective of stress axis orientation.
- 4) The Mo-Si-B alloys exhibit impressive strength retention and oxidation resistance till 1300 °C. Minor Zr addition improves oxidation-resistance in both dry and moist air.
- 5) High temperature strength and oxidation resistance, along with fracture toughness of hypo and hyper-eutectic Nb-Si-Mo alloys are significantly enhanced on Ti addition.

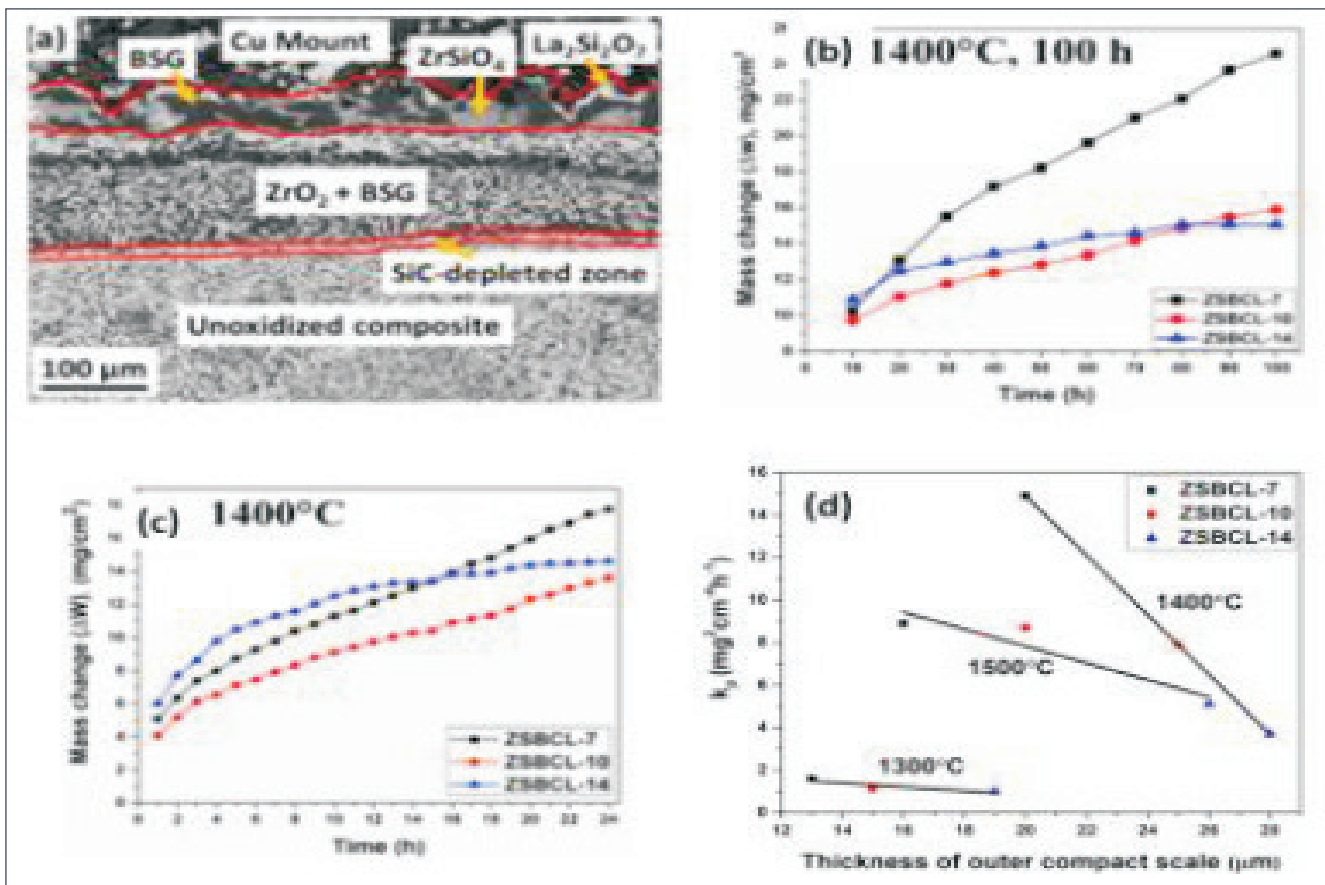


Fig. 23 : (a) SEM BSE image depicting the oxide scale formed by cyclic exposure at 1400 °C for 100 h (10 cycles of 10 h each) on ZrB<sub>2</sub>-20Si-14 LaB<sub>6</sub> composite; as well as plots depicting variation of mass gain per unit area with duration for (b) 24 cycles of 1 h exposure (24 h); (c) 10 cycles of 10 h exposure (100 h); as well as (d) variation of parabolic rate constant ( $k_p$ ) with thickness of the outer compact layer in the oxide scale in (a) [42].

6) Reinforcing with 20 vol% SiC is found optimum for ZrB<sub>2</sub> based UHTCs. The creep involves grain boundary sliding accommodated by diffusion. The oxidation resistance is noticeably improved through LaB<sub>6</sub> addition.

Whereas incremental research is in progress on metal matrix composites and Ni-based superalloys for further improvement, a significant leap forward is required for Mo and Nb-silicides to come in to practical use, considering the limitations of fabrication and limited room temperature fracture toughness. It is quite a challenge to balance the contradictory requirements of room-temperature toughening with high temperature oxidation-resistance and strength retention. Silicide coatings applied

by pack cementation on the Nb-Si based alloys have yielded promising results. Further, the observation of improved mechanical properties and oxidation resistance with Mo+Ti addition to the Nb-Si based alloys is promising. There has been an effort recently by the researchers to fabricate the ZrB<sub>2</sub>-based UHTCs with continuous C-fibre reinforcement, which has led to superior damage-tolerant behaviour.

#### Acknowledgements

The present lecture is based on the results obtained in course of dissertation research by the present and former students, Dr. Monalisa Mandal, Mr. Sumanta Bagui, Mr. Dibyendu Chakraborty, Mr. Arvind Srivastava, Dr. Sharma Paswan, Dr. Nandkishor Kumar, Dr. Kausik Chattopadhyay, Ms.

Kasturi Sala, Dr. Manab Mallik, Mr. Sabyasachi Roy and Mr. Sunil Kashyap. Sincere thanks are also due to the technical staff of the Central Research Facility and various department laboratories for help and support. The financial support from Defence Research and Development Organisation for sponsoring some of the research is also gratefully acknowledged.

## References

1. A. Mandal, R. Maiti, M. Chakraborty, and B.S. Murty, "Effect of TiB<sub>2</sub> particles on aging response of Al-4Cu alloy," *Mater. Sci. Eng. A*, vol. 386, pp. 296-300 (2004).
2. Mervin A. Herbert, Chandan Sarkar, R. Mitra and M. Chakraborty, "Microstructural evolution, hardness and alligating in the mushy state rolled cast Al-4.5Cu alloy and in-situ Al<sub>4.5</sub>Cu-5TiB<sub>2</sub> composite," *Metall. Mater. Trans. A*, vol. 38(9), pp. 2110-2126 (2007).
3. A. Jana, I.G. Siddhalingeswar, and R. Mitra, "Effect of homogeneity of particle distribution on tensile crack propagation in mushy state rolled in-situ Al-4.5Cu-5TiB<sub>2</sub> particulate composite," *Mater. Sci. Eng. A*, vol. 575, pp. 104-110 (2013).
4. Monalisa Mandal and Rahul Mitra, "Effect of pre-cold rolling on the evolution of microstructure, microtexture, and mechanical properties of the mushy state rolled in-situ Al-4.5Cu-5TiB<sub>2</sub> composite," *Mater. Char.*, vol. 146, pp. 267-278 (2018).
5. Monalisa Mandal and Rahul Mitra, "Effect of microstructure and microtexture evolution on creep behavior of hot-rolled and mushy-state rolled Al-4.5Cu-5TiB<sub>2</sub> in-situ composite," *Mater. Sci. Eng. A*, vol. 760, pp. 88-104 (2019).
6. Sumanta Bagui, Bibhu Prasad Sahu, Kinkar Laha, Soumitra Tarafder and Rahul Mitra, "Creep deformation behavior of Inconel 617 alloy in the temperature range of 650 - 800 °C," *Metall. Mater. Trans. A*, vol. 52, pp. 94-107 (2021)
7. D. Chatterjee, N. Hajari, N. Das, and R. Mitra, "Microstructure and creep behavior of DMS4-type nickel based superalloy single crystals with orientations near <001> and <011>," *Mater. Sci. Eng. A*, vol. 528, pp 604-613 (2010).
8. R. Mitra, "Mechanical Behavior and Oxidation Resistance of Structural Silicides," *Inter. Mater. Rev.*, vol. 51(1), pp. 13-64 (2006).
9. T. B. Massalski, H. Okamoto, P. R. Subramanian and L. Kacprzak (eds.): 'Binary alloy phase diagrams', Vol. 2, 1333, 1631, 2054; 1987, Materials Park, OH, ASM.
10. R. Mitra, V. V. Rama Rao and A. Venugopal Rao, "Effect of small Al alloying on microstructure and mechanical properties of molybdenum disilicide," *Intermetallics*, vol. 7(2), pp. 213-232 (1999).
11. R. Mitra and A. Venugopal Rao, "Effect of processing methods on purity and structure of internal interfaces and high temperature strength of MoSi<sub>2</sub> and MoSi<sub>2</sub>-SiC composites," *Trans. Ind. Ceram. Soc.*, vol. 60(1), pp. 12-20 (2001).
12. H. Nowotny, E. Dimakopoulou and H. Kudielka, *Monatsh. Chem.*, vol. 88, 180 (1957).
13. R. Mitra, "Silicides and Silicide Matrix Composites for High Temperature Structural Applications," in *Handbook of advanced ceramics and composites*, edited by Yashwant R. Mahajan and Roy Johnson, Springer Nature Switzerland AG 2019, pp. 1-55 (2019) [https://doi.org/10.1007/978-3-319-73255-8\\_40-1](https://doi.org/10.1007/978-3-319-73255-8_40-1)
14. M.K. Meyer, M.J. Kramer, and M. Akinc, "Oxidation behavior of boron-modified Mo<sub>5</sub>Si<sub>3</sub> at 800 -1300 °C," *Intermetallics*, vol. 4, pp. 273-81 (1996).
15. T. Hayashi, K. Ito, K. Ihara, M. Fujikura and M. Yamaguchi, "Creep of single crystalline and polycrystalline T2 phase in the Mo-Si-B system," *Intermetallics*, 12(7-9), 699-704 (2004).
16. R. Mitra, A.K. Srivastava, N. Eswara Prasad, and Sweety Kumari, "Microstructure and Mechanical Behaviour of Reaction Hot

- Pressed Multiphase Mo-Si-B and Mo-Si-B-Al Intermetallic Alloys," *Intermetallics*, vol. 14(12), pp. 1461-1471 (2006).
17. R. Mitra, K. Chattopadhyay, A.K. Srivastava, K.K. Ray, and N. Eswara Prasad, "Effect of Ductile and Brittle Phases on Deformation and Fracture Behaviour of Molybdenum and Niobium Silicide Based Composites," *Key Eng. Mater.*, vol. 395, pp. 179-192 (2009).
  18. Sharma Paswan, R. Mitra and S.K. Roy, "Oxidation Behaviour of the Mo-Si-B and Mo-Si-B-Al Alloys in the Temperature Range of 700-1300 °C," *Intermetallics*, Vol. 15, pp. 1217-1227 (2007).
  19. Barna Roy, J. Das and R. Mitra, "Transient stage oxidation behavior of  $\text{Mo}_{76}\text{Si}_{14}\text{B}_{10}$  alloy at 1150 °C" *Corr. Sci.*, vol. 68, pp. 231-237 (2013).
  20. N. K. Kumar, J. Das, and R. Mitra, "Effect of Zr addition on microstructure, hardness and oxidation behavior of arc-melted and spark plasma sintered multiphase Mo-Si-B alloys," *Metall. Mater. Trans. A*, vol. 50A, pp. 2041-2060 (2019).
  21. N.K. Kumar, J. Das and R. Mitra, "Effect of moist air and minor Zr addition on oxidation behavior of arc-melted multiphase Mo-Si-B alloys in the temperature range of 1000 °C -1300 °C," *Oxid. Met.*, vol. 93, pp. 483-513 (2020).
  22. M. E. Schlesinger, H. Okamoto, A. B. Gokhale and R. Abbaschian, "The niobium-silicon (Nb-Si) system," *J. Phase Equil.*, vol.14 (4), 502-509 (1993).
  23. W.Y. Kim, H. Tanaka, A. Kasama, R. Tanaka, and S. Hanada, "Microstructure and room temperature deformation of Nbss/Nb5Si3 in situ composites alloyed with Mo," *Intermetallics*, vol. 9, pp. 521-27 (2001).
  24. W. Li, H. Yang, A. Shan, L. Zhang, and J. Wu, "Effect of Mo addition on the phase stability of  $\beta\text{-Nb}_5\text{Si}_3$  phase," *Intermetallics*, vol. 14, pp. 392-95 (2006).
  25. K. Chattopadhyay, R Sinha, R. Mitra, and K.K. Ray, "Effect of Mo and Si on morphology and volume fraction of eutectic in Nb-Si-Mo alloys," *Mater. Sci. Eng. A*, vol. 456, pp. 358-363 (2007).
  26. K. Chattopadhyay, G. Balachandran, R. Mitra, and K.K. Ray, "Effect of Mo on Microstructure and Mechanical Behaviour of Cast Nbss-Nb5Si3 In-Situ Composites," *Intermetallics*, Vol. 14(12), pp. 1452-1460 (2006).
  27. K. Chattopadhyay, Structure-Property Relationships in Nb-Si-Mo alloys, PhD dissertation, IIT Kharagpur (2008).
  28. K. Chattopadhyay, R. Mitra, and K.K. Ray, "Non-isothermal and Isothermal Oxidation Behaviour of the Nb-Si-Mo Alloys," *Metall. Mater. Trans. A*, vol. 39A, pp. 577-592 (2008).
  29. Kasturi Sala, Swapnil A. Morankar, and Rahul Mitra, "Effect of Ti or Fe addition and annealing on microstructural evolution and mechanical properties of hypereutectic Nb-Si-Mo alloys," *Metall. Mater. Trans. A*, vol. 52, pp. 1185-1211 (2021).
  30. Kasturi Sala and Rahul Mitra, "Microstructural evolution and mechanical properties of as-cast and annealed Nb-Si-Mo based hypoeutectic alloys with quaternary additions of Ti or Fe," *Mater. Sci. Eng. A*, vol. 802, 140663 (2021).
  31. Kasturi Sala and Rahul Mitra, "Effect of Ti addition and microstructural evolution on toughening and strengthening behavior of as cast or annealed Nb-Si-Mo based hypoeutectic and hypereutectic alloys," *Metall. Mater. Trans. A*, Vol. 52, pp. 3436-59 (2021).
  32. Kasturi Sala, Sunil Kashyap and Rahul Mitra, "Effect of Ti addition on the kinetics and mechanism of non-isothermal and isothermal oxidation of Nb-Si-Mo alloys at 900 °C-1200 °C," *Intermetallics*, Vol. 138, 107338 (2021).
  33. W.G. Fahrenholtz, G.E. Hilmas, I.G. Talmy, and J.A. Zaykoski, "Refractory diborides of zirconium and hafnium," *J. Am. Ceram. Soc.*, vol. 90, pp. 1347-64 (2007).

34. A. Kumar, D. Rajdev, and D.L. Douglass, "Effect of Oxide Defect Structure on the Electrical Properties of  $ZrO_2$ ," J. Am. Ceram. Soc., vol. 55, pp. 439–45 (1972).
35. Manab Mallik, Sabyasachi Roy, K.K. Ray and R. Mitra, "Effect of SiC content, additives and process parameters on densification and structure-property relations of pressureless sintered  $ZrB_2$ -SiC composites," Ceram. Inter., vol. 39(3), pp. 2915-32 (2013).
36. I. Barin, Thermochemical Data of Pure Substances, vol. 55, 1997.
37. Manab Mallik, Ansu J. Kailath, K.K. Ray, and R. Mitra, "Effect of SiC content on electrical, thermal, and ablative properties of pressureless sintered  $ZrB_2$ -based ultrahigh temperature ceramic composites," J. Eur. Ceram. Soc., vol. 37 (2), pp. 559-72 (2017).
38. M. Suzuki, S. Sodeoka, T. Inoue, Structure control of plasma sprayed zircon coating by substrate preheating and post heat treatment, Mater Trans. JIM, vol. 46, 669–674 (2005).
39. R. Mitra, S. Upender, M. Mallik, S. Chakraborty, K.K. Ray, "Mechanical, thermal, and oxidation behaviour of zirconium diboride based ultra-high temperature ceramic composites," Key Eng. Mater., vol. 395, pp. 55-68 (2009).
40. Manab Mallik, K.K. Ray, and R. Mitra, "Effect of  $Si_3N_4$  addition on compressive creep behavior of hot pressed  $ZrB_2$ -SiC composites," J. Am. Ceram. Soc., vol. 97(9), pp. 2957-64 (2014).
41. Sunil Kumar Kashyap and Rahul Mitra, "Densification behavior involving creep during spark plasma sintering of  $ZrB_2$ -SiC based ultra-high temperature ceramic composites," Ceram. Inter., vol. 46, pp.5028-5036 (2020).
42. Sunil Kumar Kashyap, Kasturi Sala and Rahul Mitra, "Oxidation resistance and evolution of multi-layered oxide scale during isothermal and cyclic exposure of  $ZrB_2$ -SiC- $LaB_6$  composites at 1300 °C-1500 °C," Metall. Mater. Trans. A (2022) (In Press) <https://doi.org/10.1007/s11661-021-06501-4>.
43. Sunil Kumar Kashyap, Ankit Kumar and Rahul Mitra, "Kinetics and evolution of oxide scale during various stages of isothermal oxidation at 1300 °C in spark plasma sintered  $ZrB_2$  - SiC -  $LaB_6$  composites," J. Eur. Ceram. Soc., vol. 40, pp. 4997-5011 (2020)
44. Sunil Kumar Kashyap and Rahul Mitra, "Microstructure and composition of multi-layered oxide scale evolved during isothermal exposure of  $ZrB_2$ -SiC- $LaB_6$  composite to air at 1500 °C", Phil. Mag. Lett., vol. 201(7), pp. 265-276 (2021).

\*\*\*\*\*

**Adani to invest \$70 bn in renewable energy, produce cheapest hydrogen**

Billionaire Gautam Adani said his logistics-to-energy conglomerate will invest USD 70 billion over the next decade to become the world's largest renewable energy company and produce the cheapest hydrogen on the Earth. Adani Green Energy Ltd (AGEL), the world's largest solar power developer, is targeting 45 gigawatts of renewable energy capacity by 2030 and will invest USD 20 billion to develop a 2 GW per year solar manufacturing capacity by 2022-23.

Adani Transmission Ltd (ATL), India's largest private sector power transmission and retail distribution company, is looking to increase th

e share of renewable power procurement from the current 3 per cent to 30 per cent by FY 2023 and to 70 per cent by FY 2030.

*The Economic Times*

**Domestic steel prices down as iron ore, coking coal prices fall**

The domestic benchmark hot-rolled coil (HRC)

steel price has come down to around Rs 67,000 a tonne from an all-time high level of Rs 69,000-70,000 at the end of October on the back of reducing iron ore and coking coal prices.

Steelmakers such as JSW Steel and Arcelor Mittal Nippon Steel India (AM/NS), though, said the price fall since the beginning of December could be temporary as Indian steel prices are still at a discount to international prices.

Iron ore prices have come down by over 60% in the international markets, while state-owned NMDC had recently cut iron ore prices by between Rs 200 and Rs 870 a tonne for December deliveries, data from steel research and analysis firm SteelMint showed.

Coking coal prices, too, have come down from their October peak due to factors including China's decision to lift restriction on coal mining amid a power crisis, restricted buying from many Asian countries and improved supply from mines across the world. But the prices still remain much higher than, say, a year ago.

*The Economic Times*

\*\*\*\*\*

**EDITORS**

**Dr Monojit Dutta**  
**Prof J Dutta Majumdar**  
**Dr R Raghavendra Bhat**  
**Prof Sudhanshu Shekhar Singh**  
**Dr Mithun Palit**

**CORRESPONDENTS**

**Dr Chiradeep Ghosh (Jamshedpur)**  
**Sri Rishabh Shukla (Pune)**  
**Dr Ramen Datta (Delhi)**  
**Dr L Ramakrishna (Hyderabad)**  
**Sri Lalan Kumar (Visakhapatnam)**  
**Sri A S Parihar (Kanpur)**

**ADVERTISERS' INDEX**

<i>Name of the Organisations</i>	<i>Page Nos.</i>
<b>JSW Steel Ltd</b>	<b>Cover</b>
<b>Hindalco Industries Ltd</b>	<b>2<sup>nd</sup> Cover</b>
<b>Rashtriya Ispat Nigam Limited</b>	<b>5</b>
<b>Tata Steel Ltd</b>	<b>34</b>
<b>Chennai Metco Pvt Ltd</b>	<b>3<sup>rd</sup> Cover</b>

### Rourkela - Student Affiliate Chapter

The Distinguished Lecture on “Materials Science of Sustainable Metals” was organised by the Student Affiliate Chapter of IIM Rourkela Chapter on November 18, 2021 at 05:30 pm through online mode. The speaker was Prof. Dierk Raabe, Managing Director, Max-Planck-Institut fuer Eisenforschung, Germany. The introduction of the speaker was given by Prof. Anindya Basu (HOD, Metallurgical and Materials Engineering, NIT Rourkela). Various strategies for achieving sustainable metals were discussed in the



webinar. The webinar concluded with the vote of thanks by Prof. Anshuman Patra (Metallurgical and Materials Engineering, NIT Rourkela) (Faculty Advisor of Indian Institute of Metals Student Affiliate Chapter). Live streaming of the distinguished lecture was done through YouTube and the total views was above 250.

### Paloncha Chapter : NMD celebration

The IIM Paloncha Chapter celebrated the National Metallurgists’ Day on 26th November, 2021 in association with NAVA Bharat Ventures Limited. The program was started at 17:00 hrs in Lecture Hall-1. The chief guest of this occasion was Sri G. Satheesh, General Manager, Heavy Water Plant, Manuguru. The chapter Chairman Sri Y Sreenivasa Murthy presided over the occasion.

The chapter Secretary Sri V. V. Ramana Rao delivered the inaugural speech. After that the Chapter Chairman and the Chief Guest discussed on various metallurgical issues in their speech, respectively. Later on technical papers were presented by the staff of the Nava Bharat Ventures



Limited and the students from University College of engineering, Kakatiya University, Kothagudem. The mementoes were presented to the winners and runners of the quiz, elocution and technical paper presenters by the Chief Guest. The event was concluded with a vote of thanks.

### Kolkata Chapter : Webinar on “Demystifying Industry 4.0”

The IIM Kolkata Chapter along with IChE Kolkata regional Chapter and the Jadavpur University organised the webinar on “Demystifying Industry 4.0” on November 27, 2021 at 3.00 pm at the auditorium of Dr H.L. Roy Building, IChE HQ, Jadavpur University. The programme was organised in hybrid mode, wherein a number of guest speakers joined the programme in person and the rest of the guest speakers delivered their lectures through virtual mode. Mr. T V Narendran, MD Tata Steel and the President, Indian Institute of Metals graced the occasion as the Chief Guest. The key note address was delivered by Prof. Partha Pratim Chakraborty, former Director, IIT Kharagpur. Other eminent speakers were Prof. M K Jha, President IChE, Prof. C. Bhattacharjee, Pro-Vice-Chancellor, Jadavpur University and Mr. Alope Mukherjee, former Chairman, Flakt India Ltd., former Chairman CII(ER) and past President, BCCI. The speakers in the Technical Session were Mr Ambarish Dasgupta, Senior Partner, Intueriglobal.com, Mr Amitabha Sinha, TCG-Digital, Mr Nikhil Chauhan, Chief Strategy Officer, Lummus Digital, Houston and Prof. Amitava Gupta, Professor & Head(Power Engg.), J.U.

## Pune Chapter : 15th Dr Dara P Antia Memorial Lecture

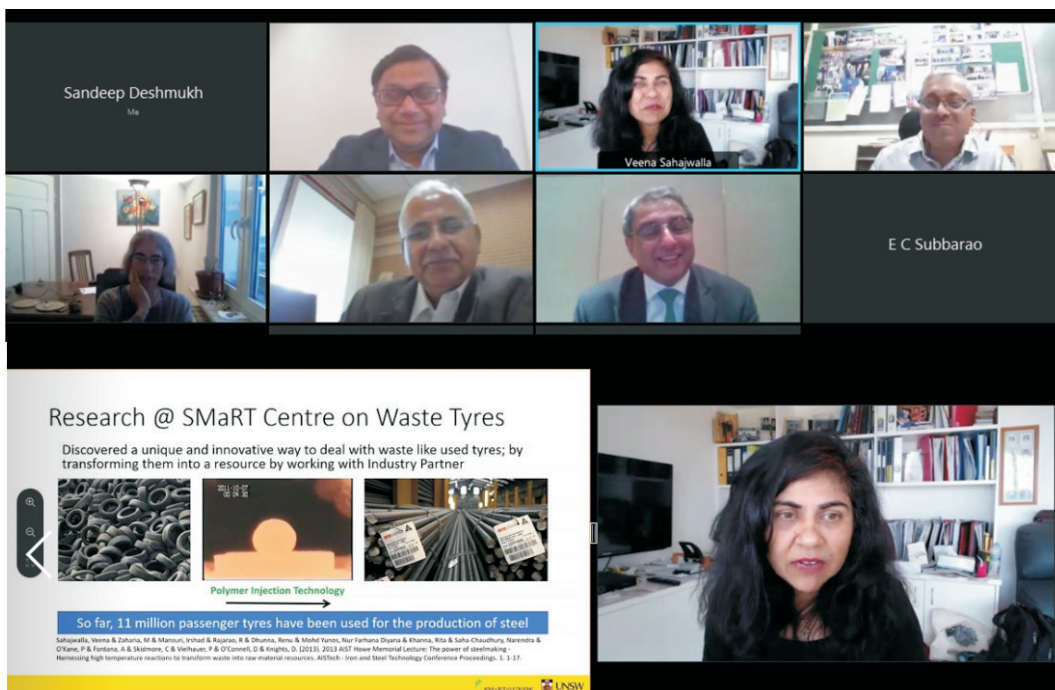
This prestigious annual national event of the Indian Institute of Metals (IIM) is organised every year by the IIM Pune Chapter and the Dr. Dara Antia Memorial Lecture Committee to commemorate the outstanding contributions and the dynamic leadership of Dr. Dara P Antia, the founder of our institute.

Professor Veena Sahajwalla Director, Centre for Sustainable Materials Research & Technology School of Materials Science & Engineering UNSW Sydney, Australia delivered the 15th Dr Dara Antia memorial lecture on December 17, 2021 in a virtual mode. Dr. Sahajwalla is the director of the ARC Industrial Transformation Research Hub for 'microrecycling', a leading national research centre that works in collaboration with industry to ensure new recycling science is translated into real world environmental and economic benefits. Professor Veena has also been appointed hub leader of the national NESP Sustainable Communities and Waste Hub. In 2021, Professor Veena featured in the ABC's Australian Story and won the 2022 Australian of the Year Awards for New South Wales <https://www.smart.unsw.edu.au/>.

During her thought-provoking lecture, she highlighted the challenges as well as the recent technological developments in the waste management and manufacturing of useful products while maintaining sustainability of the process. Some of the successful recycling methods developed are for electronic waste, textile waste, rubber tyre waste disposal for green steel manufacturing.

Mr. T V Narendran, Chairman DPA Memorial Lecture Committee, warmly welcomed the distinguished speaker, Professor Sahajwalla, the distinguished invitees, the members of IIM fraternity in India and abroad, students and all those present on this occasion. On the occasion of platinum jubilee celebration, a video film on Dr. Dara Antia was released by IIM Pune chapter to mark tribute to his outstanding contribution to material community.

A lively Q&A session was followed the wonderful lecture delivered by Prof. Sahajwalla. There were several questions from the audience both in India and abroad. Prof. Sahajwalla went into great detail about the commercialization of these innovative technologies by way of MICROfactorie™ technologies.



Professor Sahajwalla engrossed in delivering DPA memorial lecture

At the end of the Q&A session, Dr. Bhattacharjee invited Mr. Narendran, Chairman, Dr. Dara P Antia Memorial Lecture Committee to felicitate our distinguished speaker, Prof. Sahajwalla with a memento and a scroll of honour on this occasion.

A complete video recording of the lecture function is available on the IIM Pune chapter website ([www.iimpc.com](http://www.iimpc.com)) for the benefit of scientific community.

Prof. N B Dhokey, the honorary secretary of the DPA Memorial lecture committee proposed a vote of thanks on this occasion. He expressed his sincere gratitude to Prof. Sahajwalla for delivering a thought-provoking lecture as a fitting tribute to Dr. Dara Antia. He thanked Mr. Narendran, chairman, DPA Memorial Lecture committee and esteemed committee members and IIM HQ for their constant guidance and support in the organization of this prestigious event. He expressed special thanks to Dr. Debashish Bhattacharjee, VP, Tata Steel for providing all help and support in the organization of this prestigious event online this year and in facilitating our interaction with Prof. Sahajwalla. Special thanks to Mrs Mithoo Antia to grace the occasion. He also thanked all the distinguished invitees including several past presidents, several current and past members of the Dr. Dara Antia Committee and all the participants for their valuable contributions towards the success of this prestigious national event this year.

### **Keonjhar Chapter : Revival**

Among the 56 chapters in the country, the IIM Keonjhar Chapter, which had begun in 1996, had become dormant after 10 years of its inception. To revive this chapter, a program was organised

at Tata Steel Long Products premises, Bilaipada, which was participated by 34 organisational representatives and individual professional from within the District. The program was inaugurated by Mr. Ashish Anupam, Managing Director and Mr. Manikanta Naik, Sr. General Manager (Operations & Maintenance), Tata Steel Long Products Limited,



Mr. Kushal Saha, Secretary General, Indian Institute of Metals. Speaking on this occasion, the Chief Guest, Mr. Ashish Anupam emphasised on the importance of technological advancement in the country and focused on collaborative participation in overcoming the common challenges of the industries. Mr. Manikanta stressed on the need for the industries in the district to come together towards addressing common causes and felt that an institute like IIM offered the perfect platform in realising such goals. Mr. Kushal Saha shared about the illustrious background of IIM, its multifarious activities and various benefits of becoming a member of IIM. Dr. Suresh Chandra Khattoi, MD, Minmet Technologies, spoke about the advent of metals & minerals and how metal based industries in Keonjhar had grown over the years, thus improving the economy of the district. He was joined by Mr. Brij Badhadra, Executive



Vice President, JSPL who assured to extend all possible help for the revival of this Chapter.

The program concluded with a formal announcement of the revival of IIM, Keonjhar Chapter by Mr. Kushal Saha and formation of an

ad-hoc committee comprising Mr. Manikanta Naik, Mr. Brij Badhadra and Dr. Suresh Chandra Khattoi. This committee will take forward the regular activities of the Chapter and will also formulate a formal governing body.

\*\*\*\*\*

## OBITUARY



With tears in eyes and heavy heart we convey that Sri N. Rajasekaran, former VC of IIM Trichy Chapter and former DGM, BHEL, Trichy passed away on 27<sup>th</sup> December, 2021 while on a visit to New Delhi in connection with work related to some professional bodies.



It is well known that BHEL, Tiruchirappalli and its neighbourhood is a beehive of professional activities and many professional bodies work hand in hand in their pursuit of knowledge dissemination through courses, talks, seminars, exhibitions, quiz etc. While teamwork was always on display, there has been a person, who always stood out in these professional circles with his commitment, sincerity,

hard work, professionalism, planning and so on. That was Sri N. Rajasekaran, who has always been a dynamic contributor to all the professional activities in the campus.

Hailing from a remote village named Seplanatham near Neyveli, he finished his DME and joined BHEL, Trichy as a supervisor. He was soon transferred at the new Unit of BHEL at Ranipet. Working with passion there, he continued his education in parallel, and further qualified himself with AMIE and MBA. When transferred to Trichy later, he worked with great dedication as a researcher in Welding Research Institute, and later in the production shops of BHEL, and superannuated as Deputy General Manager in BHEL. As a Vice Chairman of IIM Trichy Chapter, he has driven all the activities of the Chapter with immense vigour and enthusiasm. His immense contributions and outreach would be always remembered by the fraternity.

We pray for heavenly peace of his soul.

\*\*\*\*\*

## STEEL STATISTICS

### Top 10 Steel-Producing Countries

	Dec 2021 (Mt)	% change Dec 21/20	Jan-Dec 2021 (Mt)	% change Jan-Dec 21/20
China	86.2	-6.8	1,032.8	-3.0
India	10.4	0.9	118.1	17.8
Japan	7.9	5.4	96.3	14.9
United States	7.2	11.9	86.0	18.3
Russia	6.6 e	0.0	76.0	6.1
South Korea	6.0	1.1	70.6	5.2
Turkey	3.3	-2.3	40.4	12.7
Germany	3.1	0.1	40.1	12.3
Brazil	2.6	-11.4	36.0	14.7
Iran	2.8 e	15.1	28.5	-1.8

e - estimated. Ranking of top 10 producing countries is based on year-to-date aggregate

Source : worldsteel.org

**1.5 tonnes  
of CO<sub>2</sub>**

1.4 tonnes of Iron Ore, 740 Kg of Coal  
and 120 Kg of Limestone.

Source: World Steel Association

# RECYCLING STEEL FOR A BETTER TOMORROW

Steel Production through Electric Arc Furnace (EAF) uses scrap as an input & Tata Steel has set up India's first state-of-the-art scrap processing centre at Rohtak, Haryana. The scrap is sourced from market segments like End-of-Life Vehicle scrap, Obsolete Household Scrap, Industrial Scrap etc through Digital FerroHaat App.

Sure we make steel.

**But #WeAlsoMakeTomorrow.**



Tata Steel is now a part of ResponsibleSteel™, the industry's first global multi-stakeholder standard and certification initiative.

[www.wealsomaketomorrow.com](http://www.wealsomaketomorrow.com) |      | [www.tatasteel.com](http://www.tatasteel.com)



**World Class Products**  
Made in India - Exported worldwide

*Microstructure  
Analysis for  
QC and Research.*



**Chennai Metco**

[www.chennaimetco.com](http://www.chennaimetco.com)

STEEL FACTS

Remanufactured engines  
can be produced with up to

83%

less energy than the energy  
needed to produce a new engine,  
and emitting up to 87% less CO<sub>2</sub>.  
Consumers can also save up to  
53% on cost over a new engine.

worldsteel.org